The Astrophysical Journal, 699:1067–1086, 2009 July 10 doi:10.1088/0004-637X/699/2/1067

SPITZER MID-IR SPECTRA OF DUST DEBRIS AROUND A AND LATE B TYPE STARS: ASTEROID BELT ANALOGS AND POWER-LAW DUST DISTRIBUTIONS

Farisa Y. Morales[1,2], M. W. Werner[1], G. Bryden[1], P. Plavchan[3], K. R. Stapelfeldt[1], G. H. Rieke[4], K. Y. L. Su[4], C. A. Beichman[1,3], C. H. Chen[5], K. Grogan[1], S. J. Kenyon[6], A. Moro-Martin[7], and S. Wolf[8]
[1] Jet Propulsion Laboratory, California Institute of Technology, 4800 Oak Grove Drive, Pasadena, CA 91109, USA; Farisa@jpl.nasa.gov
[2] Department of Physics and Astronomy, University of Southern California, Los Angeles, CA 90089-0484, USA
[3] NASA Exoplanet Science Institute (NExScI), California Institute of Technology, 770 S. Wilson Ave, Pasadena, CA 91125, USA
[4] Steward Observatory, University of Arizona, 933 North Cherry Avenue, Tucson, AZ 85721, USA
[5] Space Telescope Science Institute (STScI), 3700 San Martin Drive, Baltimore, MD 21218, USA
[6] Harvard-Smithsonian Center for Astrophysics, 60 Garden Street, Cambridge, MA 02138, USA
[7] Department of Astrophysical Sciences, Princeton University, Princeton, NJ 08540, USA
[8] Institut für Theor. Physik und Astrophysik, Christian-Albrechts-Universitaet zu Kiel, Leibnizstr. 15, 24118 Kiel, Germany
Received 2008 December 16; accepted 2009 April 24; published 2009 June 18

ABSTRACT

Using the *Spitzer*/Infrared Spectrograph (IRS) low-resolution modules covering wavelengths from 5 to 35 μm, we observed 52 main-sequence A and late B type stars previously seen using *Spitzer*/Multiband Imaging Photometer (MIPS) to have excess infrared emission at 24 μm above that expected from the stellar photosphere. The mid-IR excess is confirmed in all cases but two. While prominent spectral features are not evident in any of the spectra, we observed a striking diversity in the overall shape of the spectral energy distributions. Most of the IRS excess spectra are consistent with single-temperature blackbody emission, suggestive of dust located at a single orbital radius—a narrow ring. Assuming the excess emission originates from a population of large blackbody grains, dust temperatures range from 70 to 324 K, with a median of 190 K corresponding to a distance of 10 AU. Thirteen stars however, have dust emission that follows a power-law distribution, $F_\nu = F_0\lambda^\alpha$, with exponent α ranging from 1.0 to 2.9. The warm dust in these systems must span a greater range of orbital locations—an extended disk. All of the stars have also been observed with *Spitzer*/MIPS at 70 μm, with 27 of the 50 excess sources detected (signal-to-noise ratio > 3). Most 70 μm fluxes are suggestive of a cooler, Kuiper Belt-like component that may be completely independent of the asteroid belt-like warm emission detected at the IRS wavelengths. Fourteen of 37 sources with blackbody-like fits are detected at 70 μm. The 13 objects with IRS excess emission fit by a power-law disk model, however, are all detected at 70 μm (four above, three on, and six below the extrapolated power law), suggesting that the mid-IR IRS emission and far-IR 70 μm emission may be related for these sources. Overall, the observed blackbody and power-law thermal profiles reveal debris distributed in a wide variety of radial structures that do not appear to be correlated with spectral type or stellar age. An additional 43 fainter A and late B type stars without 70 μm photometry were also observed with *Spitzer*/IRS; results are summarized in Appendix B.

Key words: circumstellar matter – infrared: stars – planetary systems: formation – stars: individual (HD 1404, HD 10939, HD 23267, HD 23642, HD 23763, HD 24141, HD 24817, HD 28355, HD 30422, HD 32977, HD 37286, HD 38056, HD 38206, HD 70313, HD 71722, HD 74873, HD 79108, HD 80950, HD 87696, HD 92536, HD 93738, HD 98673, HD 110411, HD 115892, HD 125283, HD 126135, HD 128207, HD 132238, HD 135379, HD 135454, HD 136246, HD 136347, HD 136482, HD 137015, HD 138923, HD 138965, HD 141378, HD 142139, HD 145964, HD 153053, HD 159170, HD 159492, HD 166046, HD 182919, HD 183324, HD 191174, HD 192425, HD 196544, HD 215766, HD 220825, HD 223352, HD 225200)

Online-only material: color figures

1. INTRODUCTION

Spitzer Space Telescope (Werner et al. 2004) observations have greatly enriched our understanding of disks of dust around main-sequence stars that are associated with planetary systems or planetary system formation (Werner et al. 2006). The argument for this association is quite simple: the observed particles have short lifetimes against various dissipation mechanisms in comparison to the age of their parent stars; therefore, the dust must be replenished through processes such as the grinding down of asteroids or evaporation of comets in each system. By studying these debris disks, it is possible to probe the underlying planetary systems.

The spatial distribution of orbiting dust can be used to determine the location of parent planetesimals and, potentially, the influence of unseen planets. *Spitzer* and *Hubble Space Telescope* resolved imaging of nearby debris disks, for example, reveal a wide variety of disk structures (e.g., Su et al. 2005; Kalas et al. 2006). Circumstellar matter can be located in narrow rings or in continuous disks with material spread over a broad range of radii. Of particular interest, the extremely well-defined ring around Fomalhaut is offset onto an eccentric orbit, suggesting the presence of a shepherding planet (Stapelfeldt et al. 2004; Kalas et al. 2005), which has recently been directly observed by Chiang et al. (2009).

The debris disk architecture is a fundamental clue to the nature of the underlying planetary system. However, relatively few debris disks can be resolved with current instruments. Instead, we have to use the spectral energy distributions (SEDs) to infer indirectly the radial distribution of the dust in unresolved

systems. Here, we use SEDs based on observations with the *Spitzer* Infrared Spectrograph (IRS; Houck et al. 2004) and Multiband Imaging Photometer (MIPS; Rieke et al. 2004) to explore disk architecture.

As the basis for this work, we rely on previous *Spitzer* surveys that have successfully identified large numbers of stars with infrared excesses. For example, a large number of nearby A stars were observed by *Spitzer*/MIPS at 24 μm (Rieke et al. 2005) later supplemented with 70 μm photometry (Su et al. 2006). At both wavelengths, more than 30% of the systems exhibit stronger emission than expected from the stellar photosphere alone, i.e., the stars have infrared excesses due to surrounding dust. This detection rate for IR excess is much higher than for main-sequence solar-type stars ($\sim$15%; Bryden et al. 2006; Trilling et al. 2008) or for low-mass M stars (<10%; Gautier et al. 2007; Plavchan et al. 2009). This high detection rate around A stars readily provides us with a large sample of debris disks for further study. We have identified a sample of 52 A and late B type stars with IR excesses that are bright enough for spectroscopic follow-up with IRS.

For our target sample (defined in Section 2), we first describe the data reduction for the set of IRS and MIPS observations (Section 3). In Section 4, we present the data analysis, where we disentangle the dust emission from the stellar photosphere. In Section 5 we constrain disk properties such as the optical depth distribution (τ(R)), dust mass ($M_{\rm dust}$), and fractional luminosity ($L_{\rm dust}/L_*$) and we look for correlations of the disk properties with stellar age. We discuss the implication of these results in Section 6 and summarize our findings in Section 7.

2. SAMPLE SELECTION

Our target sample comes from two *Spitzer*/MIPS Guaranteed Time surveys for debris disks around nearby stars. About half of our stars (27 of 52) come from a program designed to study main-sequence A-type stars identified based on their position on the Hertzsprung–Russell (H–R) diagram (Chen et al. 2005; C. H. Chen et al. 2009, in preparation). The specific selection criteria are that the stars be nearby ($d < 80$ pc), A type ($0.0 < B - V < 0.2$ mag), and main sequence ($M_V > 1.0 + 5.5(B - V)$; Jura et al. 1998). The remaining 25 stars in our sample come from a large survey of 266 main-sequence A-type stars, some with MIPS 24 μm excess and some with indications of flux excesses detected at *IRAS* 25 μm (Rieke et al. 2005). Stellar masses in the Rieke sample range from $\sim$1.5 to 2.5 $M_\odot$ and ages from $\sim$5 to 850 Myr. In order to study the evolution of IR excess, this survey concentrated in particular on members of young clusters with relatively well-known ages, resulting in a greater sampling of the young end of the age range.

From both of these surveys, we consider the sample of stars identified as having IR excesses at MIPS 24 μm that also have 70 μm detections or upper limits. Table 1 lists the spectral type, age, and distance for the resulting sample of 52 main-sequence A and late B type stars. The stars in our entire sample are located 18–192 pc away with ages from <5 to $\sim$1000 Myr, where age estimates are either from cluster and moving group membership or are found by comparing the stars' positions on the H-R diagram with isochrones as described by Rieke et al. (2005). The ratio of the reported 24 μm flux to that expected from the stellar photosphere ($F_{24\,\mu{\rm m}}/F_\star$) is also listed in Table 1, with fluxes ranging from 1.2 to >4 times that expected from the stellar photosphere.

In addition to our 52-star core sample, we have obtained spectra for an additional 42 sources (35 faint cluster-member targets with MIPS 24 μm data and seven *IRAS*-25-μm-selected objects) which lack 70 μm photometry. The results from these lower quality spectra are summarized in Appendix B.

3. OBSERVATIONS AND DATA REDUCTIONS

3.1. IRS Spectra

All stars were observed with the low spectral resolution modules of the IRS spectrograph ($\lambda/\Delta\lambda\sim$100), which cover the wavelength range from 5.2 to 35.0 μm. Each spectrum contains four components—two orders from the Short-Low module (SL; 5.2–14.5 μm) and two from Long-Low (LL; 14.0–35.0 μm). Most of our target stars were observed under a single *Spitzer* program (PID 20132), with observation strategy based on the measured 24 μm flux: 36 sources with $F_{\nu,24} > 100$ mJy (SL: 2 cycles of 14 s exposures per order, and LL: 2 cycles of 30 s per order) and 10 sources with 20 mJy $< F_{\nu,24} <$ 100 mJy (SL: 1 cycle of 60 s per order, and LL: 4 cycles of 120 s per order). To position the target star in the slit, high-accuracy red or blue self peak-up was used. Six stars were observed within a separate program (PID 41) with a similar strategy, yielding comparable quality spectra.

The bulk of the data reduction was carried out with the *Spitzer* Science Center's IRS data reduction pipeline version S15.3.0. We use post-basic calibrated data (post-BCDs) in which the spectra, under standard procedure, are extracted using a variable aperture width that scales with the width of the instrumental point-spread function. The co-added spectra are calibrated assuming a point source, and background-subtracted by differencing the two nodding positions (see the IRS manual for further details). Beyond the post-BCD spectra, we have performed several additional data reduction and analysis steps using IDL—cleaning bad-pixel data, averaging extracted spectra from both nodding positions, stitching modules together using overlap regions, and trimming the low-quality edges.

The observed brightness of the IRS spectrum can vary depending on the target's position in the slit, resulting in an IRS calibration uncertainty of up to $\sim$10% for the low-resolution modules (IRS pipeline handbook). Therefore, we choose to scale all spectra to their corresponding MIPS 24 μm photometric point which has a better calibration accuracy of $\sim$2% (Engelbracht et al. 2007); each spectrum is convolved with the MIPS 24 μm filter response function and then normalized to the MIPS value.

The SED shape is crucial to our study. Unfortunately some of the SL1 data (7.5–14.5 μm) suffer from a spectral curvature effect caused by pointing mismatches between the slit and the target. The slit-loss varies as a function of the chromatic PSF leading to a concave shape within the SL1 spectrum and to order mismatches between SL1 and LL2 when using high accuracy self peak up (see "Low-Res Nonrepeatability" and "Curvature in SL1" on the SSC's IRS Instrument Data Features/Caveats Web site for further details). In almost all cases, any loss of flux is negligible after the orders are stitched together. For the two most severely affected spectra we increase the SL1 error values by $\sim$2% of the flux in order to account for the error introduced. Given that we have spectral measurements at both ends of the SL1 order via SL2 and LL2, and that we use a minimum χ^2 procedure to fit to the entire IRS spectra, the estimated uncertainties due to this effect is small relative to

Table 1
Stellar Sample and Properties

HD	H–R	Name	Spectral Type	V (mag)	Age[l] (Myr)	Distance (pc)	$F_{24\,\mu m}/F_\star$	IRS AOR
001404[a]	68	ZI 7, σ And	A2V	4.52		43.3	1.29	14160384
010939	520	q02 Eri	A1V	5.03	320	57.0	1.59	14139392
023267			A0	6.88	80	136.4	3.58	14148096
023642[b]		V1229 Tau	A0V	6.83	125	110.4	1.33	14149888
023763[c]			A1V	6.96	125	144.9	1.10	14150144
024141	1192		A5m	5.78		52.2	1.43	14160640
024817	1224		A2Vn	6.08	400	75.4	1.59	14139648
028355[c]		b Tau	A7V	5.02	625	49.2	1.35	14146816
030422[a]		EX Eri	A3IV	6.18	10	57.5	1.41	14147584
032977	1658	l Tau	A5V	5.29	850	53.2	1.47	14139904
037286	1915		A2III-IV	6.26		56.6	2.32	14140160
038056			A0V	5.34	250	132.5	2.25	12713728
038206			A0V	5.73	9	69.2	4.01	12713472
070313	3277		A3V	5.51	300	51.4	1.70	14140416
071722	3341		A0V	6.05	100	71.1	2.16	14140672
074873	3481	50 Cnc	A1V	5.89	100	61.1	1.73	14140928
079108			A0V	5.14	320	115.2	2.05	12710400
080950			A0V	5.87	80	80.8	4.09	12720640
087696[d]	3974		A7V	4.48	900	27.9	1.29	14141184
092536[c]			B8V	6.31	50	147.1	3.09	14147328
093738[c]			B9.5V	6.45	50	143.9	1.47	14149376
098673	4388		A7Vn	6.43	1000	78.2	1.73	14141440
110411[d]		ρ Vir	A0V	5.87	10	36.9	1.66	12720384
115892[e]	5028	ι Cen	A2V	2.70	350	18.0	1.20	14144512
125283	5357		A2Vn	5.93	100	68.5	1.34	14141696
126135			B8V	6.96	15	155.5	2.71	14148608
128207			B8V	5.73	15	128.5	1.21	14149120
132238			B8V	6.47	15	191.9	2.40	14148352
135379	5670	β Cir	A3V	4.06	600	29.6	1.73	14141952
135454			B9V	6.75	15	137.2	1.44	14150656
136246			A1V	7.17	15	143.5	1.34	14151168
136347[f,k]			A0sp...	6.53	15	123.5	...	14150400
136482			B8/B9V	6.53	15	124.5	3.53	14147840
137015[g]			A2V	6.64	15	146.6	1.26	14150912
138923[a]		ZI 1138, FIN 231AB	B8V	7.03	15	112.5	3.46	14147072
138965	5792		A1V	6.25	100	77.3	3.83	14142208
141378	5875		A5IV	6.42	150	49.2	1.49	14142720
142139[h]	5905		A3V	5.53	700	66.0	1.61	14142464
145964			B9V	5.75	5	105.8	1.14	14149632
153053[f]	6297		A5IV-V	6.41	800	50.7	1.25	14160896
159170	6534		A5V	5.64	800	48.4	1.53	14142976
159492	6549		A5IV-V	5.61	170	42.2	2.41	14143232
166046[f,k]	6782		A3V	5.25	200	50.9	...	14161920
182919[c]	7390	5 Vul	A0V	5.90	100	66.9	1.74	14143488
183324[d]		35 Aql, c Aql	A0V	5.59	10	59.0	1.21	14148864
191174[f]	7695		A2II-III	5.79		78.5	1.92	14161152
192425	7724	ρ Aql	A2V	6.26	120	47.1	1.71	14143744
196544[i]	7883		A2V	4.94		54.3	1.63	14161408
215766[f]	8673	69 Aqr	B9V	5.42	100	79.7	1.97	14144000
220825[j]	8911	κ Psc	A0p...	5.67	150	49.7	1.67	14144256
223352	9016	δ Scl	A0V	4.92	100	44.0	1.61	14161664
225200			A0V	4.57	90	129.0	1.73	12720128

Notes.
[a] Variable star.
[b] Eclipsing binary of Algol type.
[c] Star in cluster.
[d] Variable star of delta Sct type.
[e] High proper-motion star.
[f] Star in double system.
[g] Double or multiple star.
[h] Star suspected of variability.
[i] Spectroscopic binary.
[j] Variable star of alpha2 CVn type.
[k] No detectable 24 μm excess; preliminary result confused by close companion.
[l] Age estimates as in Rieke et al. (2005).

the overall IRS calibration uncertainty and do not affect our qualitative results.

3.2. MIPS Photometry

Our 52 star sample is defined based on *Spitzer*/MIPS 24 μm observations. All of the target stars have been observed by MIPS at both 24 and 70 μm and were initially identified as having IR excesses at 24 μm (stars without 70 μm observations are relegated to Appendix B). While the results of these photometric measurements have already been published, they do not come from a single program - about half are from Chen et al. (2005; C. H. Chen et al. 2009, in preparation) and half from Rieke et al. (2005) and Su et al. (2006). Therefore, we re-reduced all MIPS data for uniformity. Basic data reduction procedures can be found in Engelbracht et al. (2007) and Gordon et al. (2007) for 24 and 70 μm, respectively. Since all the sources are expected to be unresolved, we use PSF extraction to estimate the photometry. All sources are detected at 24 μm. For 70 μm targets that failed in PSF fitting, we obtained the upper limits using aperture photometry centered at the detected 24 μm positions, consistent with the telescope pointing accuracy of $<1''$ (Werner et al. 2004). The results are listed in Table 3 and are discussed in more detail in Section 4.2.

4. RESULTS AND ANALYSIS

4.1. IRS Spectra

Significant IRS excess was detected in all but two systems—HD 136347 and HD 166046. We found that these two sources were incorrectly classified as possessing 24 μm excesses. We attribute the apparent excesses to binary companions with separations of $6''$ and $14''$, respectively. The false excesses arise from early use of aperture photometry with relatively large apertures. For both systems, simultaneously fitting the PSFs of the stellar components finds 24 μm fluxes that are photospheric; the spurious excess is from the companion stars. Overall, however, the MIPS 24 μm measurements are robust, with 50 of 52 excesses confirmed by the IRS spectra. Even in cases where the photometric excess is only $\sim$10%, the shape of the spectrum as measured by IRS clearly shows dust emission above the photospheric contribution. Because our target stars were chosen based on their 24 μm emission, it is not surprising that our detection rate for IR excess is higher than in a blind survey (e.g., 12% with IRS for solar-type stars; Lawler et al. 2009). Chen et al. (2006) report a similar IRS survey of disks detected by *IRAS* at 60 μm; only 56% have detected excesses at 24 μm.

4.1.1. SED Fitting Procedure

The spatial distribution of dust within debris disks varies considerably from system to system. Some systems exhibit a well-defined ring of orbiting material, e.g., HR 4796A (Koerner et al. 1998; Schneider et al. 1999) and Fomalhaut (Kalas et al. 2005). Others reveal a grain spatial distribution extending over a wide range of radii, e.g., β Pic, (Heap et al. 2000; Golimowski et al. 2006) and Vega (Su et al. 2005). Motivated by the shape of the excess spectra, and the known variety of disk architectures, we consider two simple models for fitting the dust emission seen by IRS—a single temperature blackbody or a power-law flux distribution. The specific equations that we fit are

$$F_\nu = c_{1\star}\mathrm{NG}(T_\star) + c_{1d}\,B_\nu(T_{\mathrm{dust}}), \quad (1)$$

$$F_\nu = c_{2\star}\mathrm{NG}(T_\star) + c_{2d}\lambda^\alpha, \quad (2)$$

where the first terms (NG(T_*)) are the emission from a NextGen stellar photosphere of stellar temperature (T_*) fixed by spectral type (Table 1), and the second terms are from the dust. The first model can be thought of as a star with a ring of dust that achieves a single equilibrium temperature based on its distance from the star (Equation (1) assumes large grains, for no emissivity effects are included). Equation (2) is a star with a continuous disk model where the dust flux density varies as wavelength to the power α. Each of our models has three free parameters: the normalization of the stellar photosphere ($c_{1\star}$ or $c_{2\star}$), the normalization of the dust component (c_{1d} or c_{2d}), and either the dust temperature (T_{dust}) for model 1, or the spectral slope (α) for model 2.[9] For the stars that we know to have 24 μm excess, it is important to leave the normalization of the stellar photosphere a free parameter in order to allow identification of excess emission at the shortest IRS wavelengths.

Finally, our best-fit model (of the form 1 or 2 above) is selected based on the best reduced χ^2. The best-fit χ^2 values range between 0.5 and 10.6. All fitting parameters resulting from our simple model fits are listed in Table 2. Figure 1 shows paradigm examples of the two classes of objects. The SEDs for two systems, HD 80950 and HD 10939, are shown along with the best-fit blackbody (red) and the best-fit power law (blue) for each object. The stellar photospheres are shown in gray and the IRS spectra in black. A posteriori we find our fits for all stars consistent with Two Micron All Sky Survey (2MASS) *JHKs* photometry, as plotted in Figure 1.

In some cases, the difference between blackbody and power-law excess is clear; for instance, the IRS data for HD 80950 (Figure 1; left panel) is much better fit by a blackbody while HD 10939 (right) is better fit by a power law (note that in this case the extrapolation of the IRS power law agrees with the MIPS 70 μm and *IRAS* 100 μm photometric measurements). Figure 2 shows the power law versus blackbody reduced χ^2 values for the overall sample. Sources above the diagonal dashed line have IRS excess profiles better fit by a single temperature blackbody, while power-law flux distributions are below. Excess systems better fit by power laws have reasonably good fits, with average χ^2(power law) of 1.4. Some systems emitting blackbody-like at IRS wavelengths, however, still do not have good fits, with χ^2(blackbody) as high as 15. Close examination of spectra for objects with the largest χ^2(blackbody) values suggest that the systems are not well fit by either a blackbody or a power law and that either additional disk structure (e.g., HD 28355), or faint spectral features may be evident (HD 159492).

Interestingly, in the compilation by Chen et al. (2006) blackbody and power-law spectra are also evident. Examples of the latter class are HR 333, 49 Cet, γ Tri, and γ Oph. Chen et al. (2006) constrained their power-law fits to have unity slope, and the fits for this SED shape were poor; the power laws in the Chen et al. (2006) sample appear to be much steeper, comparable to the steepest examples in our sample.

[9] Five combinations of components were initially attempted. Models 3–5 were three-component combinations of a NextGen stellar photosphere plus, a blackbody and a power law, two blackbodies, or two power laws, respectively. In all cases, the inclusion of an additional component resulted in a confidence value for the *F*-test statistic of less than 99%, thus the two-component models are chosen in preference to three-component models. The *F*-test, designed to compare two population variances, considers the ratio of the two- vs. three-component χ^2 variables divided by their respective degrees of freedom.

Table 2
Fitting Parameters

HD	$c_{1\star}$	c_{1d}	$T_{\rm dust}$ (K)	Blackbody Best Reduced χ^2	$c_{2\star}$	c_{2d}	Slope α	Power Law Best Reduced χ^2
001404	1.000	2.442	185	3.8	0.991	2.8E-05	0.9	4.5
010939	1.002	19.818	133	5.7	0.993	2.5E-06	1.9	2.1
023267	1.008	9.859	181	1.4	0.962	1.1E-04	1.2	1.7
023642	0.988	40.786	102	1.4	0.987	0.0E+00	3.3	1.6
023763	0.995	208.148	71	3.3	0.964	8.3E-03	1.3	5.3
024141	1.008	1.828	216	1.4	0.990	1.5E-04	0.5	1.4
024817	1.003	1.187	276	1.0	0.966	8.8E-04	0.1	1.2
028355	0.970	24.846	113	10.6	0.968	1.0E-07	2.8	12.4
030422	0.995	6.454	161	1.7	0.987	8.7E-06	1.4	1.7
032977	0.996	3.266	187	1.9	0.984	3.5E-05	1.0	3.4
037286	1.001	7.243	187	1.0	0.967	2.3E-04	0.7	1.0
038056	1.038	27.439	139	1.8	0.997	4.7E-05	1.2	1.5
038206	1.034	14.659	171	6.5	0.952	2.0E-04	1.1	1.2
070313	1.013	11.253	152	3.7	1.000	8.3E-06	1.6	2.3
071722	1.021	27.272	137	3.2	1.004	6.0E-06	1.9	1.0
074873	1.012	4.407	190	1.3	0.991	1.3E-04	0.8	1.3
079108	1.037	15.418	144	1.9	1.002	5.4E-05	1.2	1.4
080950	1.015	9.065	188	2.1	0.904	5.5E-04	0.8	2.3
087696	0.995	2.551	182	4.9	0.984	3.1E-05	0.9	7.9
092536	1.014	3.328	251	1.2	0.698	8.0E-03	0.2	1.6
093738	1.005	1.205	265	2.4	0.959	1.4E-03	0.1	3.6
098673	1.000	4.363	193	1.1	0.979	8.6E-05	0.9	1.3
110411	1.021	45.309	111	2.6	1.009	2.1E-06	2.0	1.1
115892	0.980	1.509	190	5.8	0.966	9.3E-05	0.4	10.5
125283	1.018	2.485	194	5.2	1.006	6.3E-05	0.8	5.9
126135	0.995	5.123	209	1.3	0.940	3.6E-04	0.7	1.4
128207	0.992	1.694	193	3.6	0.986	2.7E-05	0.9	5.0
132238	1.004	3.607	240	1.2	0.938	8.6E-04	0.4	1.3
135379	1.001	6.420	172	5.2	0.979	6.8E-05	0.9	10.9
135454	0.989	0.715	324	1.2	0.934	3.4E-03	0.4	1.3
136246	1.000	5.584	159	1.0	0.993	9.2E-06	1.4	1.3
136482	1.013	5.907	209	1.2	0.930	6.4E-04	0.6	1.4
137015	0.989	0.000	224	1.2	0.978	1.1E-04	0.5	1.6
138923	1.011	2.173	286	1.0	0.813	6.4E-03	0.1	2.4
138965	1.028	87.293	119	10.6	0.999	3.0E-06	2.4	1.2
141378	1.006	22.520	123	3.2	0.999	1.0E-06	2.2	1.6
142139	1.004	5.788	177	1.2	0.975	6.7E-05	0.9	1.2
145964	0.994	21.765	98	1.8	0.994	1.0E-07	2.4	1.9
153053	0.995	30.169	105	3.7	0.993	1.0E-07	2.9	3.0
159170	1.005	2.648	209	1.8	0.983	1.4E-04	0.6	2.1
159492	1.005	11.927	161	9.8	0.976	3.6E-05	1.3	14.5
182919	0.993	3.630	206	1.5	0.968	1.5E-04	0.7	1.5
183324	0.979	8.965	126	4.5	0.977	3.0E-07	2.2	5.2
191174	0.996	1.895	260	1.6	0.934	1.4E-03	0.1	1.7
192425	1.005	5.004	186	3.5	0.984	7.0E-05	0.9	3.6
196544	1.011	6.704	169	2.7	0.998	2.1E-05	1.3	2.4
215766	0.999	7.089	187	1.4	0.975	7.5E-05	1.0	1.6
220825	0.996	3.270	204	3.5	0.972	1.4E-04	0.7	6.6
223325	0.997	3.925	192	2.9	0.971	1.1E-04	0.8	5.9
225200	1.036	9.022	163	1.8	1.011	5.8E-05	1.0	1.2

Notes. The normalization of the stellar photosphere, $c_{1\star}$ or $c_{2\star}$, is a multiplicative factor to an initial normalization from the norm of the first 10 IRS pixel values in SL2. The normalization of the dust component c_{1d} or c_{2d}, is a multiplicative factor to an initial normalization to the MIPS 24 μm photometry. The dust temperature, $T_{\rm dust}$, is allowed to vary from 5 to 500 K, and the spectral slope, α, from 1.0 to 10.0. All normalization factors are allowed to vary between 10^{-5} and 10^{2}.

4.1.2. Fitting Results

Our data suggests two different inner disk architectures. At the IRS wavelength range, the shape of the flux distribution differs significantly for the two types (Figure 1). The majority of star–disk systems fit the basic architecture of a narrow ring described by Equation (1). Yet, a quarter (13 systems) of our sample are better explained by Equation (2), where a broad radial distribution of grains produces a superposition of blackbodies and the thermal component increases linearly (in log space) as a function of wavelength. The photosphere-subtracted IRS excess flux, the best-fit model, and the MIPS 70 μm residuals (data with photosphere subtracted) are plotted in Figure 3.

Spitzer is probing warm regions similar in temperature to our asteroid belt—where typical temperatures range from 200 K at

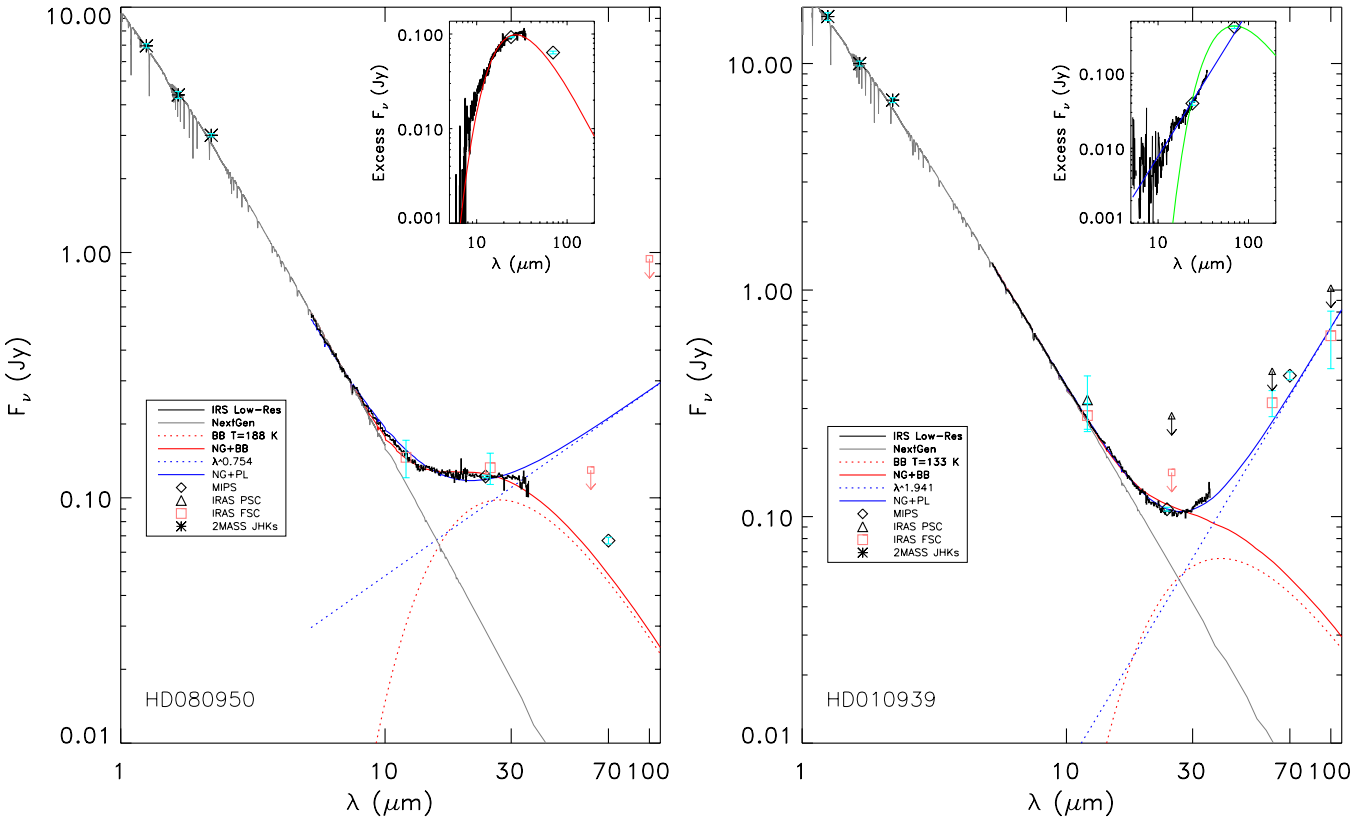

Figure 1. SEDs for two objects in our sample—HD 80950 (left) and HD 10939 (right). The former is an example of a blackbody-like disk SED, while the latter is a power-law SED. 2MASS *JHKs* fluxes (Cutri et al. 2003) are plotted as asterisks with cyan error bars. Color-corrected *IRAS* point-source data, faint source data, where available, and MIPS photometry are shown in black triangles, red squares, and black diamonds, respectively, with cyan error bars, and/or down arrows for upper limits. Our *Spitzer* IRS spectra are shown in solid black. Overlaid in gray are the best-fit NextGen stellar atmosphere models resulting from fitting procedure described in Section 4.1.1. For both objects, the best-fit blackbody and power-law models are plotted in red and blue dotted lines, respectively; and the sum of photosphere plus thermal model in solid red and blue. The small insert plots on the upper right corners are the photosphere subtracted excess flux vs. wavelength based on best minimum χ^2 fits.

2.2 AU down to 165 K at 3.2 AU from the Sun (Low et al. 1984). The blackbody temperatures found after χ^2 fitting the IRS data range from 70 to 324 K, with a median dust temperature of 190 K (see Table 3). ∼75% of the fits consistent with a single-temperature blackbody exhibit flux excesses shortward of 10 μm. For sources where the IRS data is best fit by a power law, temperatures corresponding to emission at ∼10 to 35 μm range from ∼365 to 105 K. All spectra best fit by a power-law flux distribution model have positive slopes; furthermore, among power-law spectra we find significant diversity in slope, $1.0 \leqslant \alpha \leqslant 2.9$ (see Table 3).

4.1.3. Spectral Features

None of the spectra in our sample display prominent spectral features[10] at the observed wavelengths. The lack of spectral features is likely due in part to a lack of small dust grains. The particle radius above which grains tend to have constant emissivity is $2\pi a_{\rm grain} \gtrsim \lambda$ for strongly absorbing material (Bohren & Huffman 1983; Backman et al. 1992). Grains small enough to produce spectral features at IRS wavelengths ($2\pi a_{\rm grain} \leqslant \lambda_{IRS}$) are generally blown out of the system on an orbital timescale. This blowout explanation is consistent with observations of solar-type stars which have smaller blowout radii; there the handful of known warm dust systems (those with 10 μm excesses) do have spectral features (e.g., HD 69830; Beichman et al. 2005a).

The blowout radius is given by (Plavchan et al. 2009)

$$a_{\rm BOS} = \frac{3}{8\pi}\frac{L_\star}{M_\star}\frac{Q_{\rm rad}}{Gc}\frac{1}{\rho_{\rm grain}}, \quad (3)$$

where $L_\star$ and $M_\star$ are the stellar luminosity and mass. G is the gravitational constant. $Q_{\rm rad}$ is the radiation pressure coefficient averaged over the stellar spectrum. Since the radiation from A-type stars is dominated by ultraviolet and optical light ($2\pi a/\lambda \gg 1$), the effective cross sections of the grains are approximately their geometric cross sections. ρ is the density of individual grains, which we take to be 3.0 g cm^{-3} for typical silicate particles. Under the above assumptions, we find blowout sizes for the stars in our sample ranging from 2 μm for A7 stars with luminosity 10.5 $L_\odot$ to 16 μm for B8 stars with luminosity 180 $L_\odot$. Blowout radii for each of our target stars are listed in Table 3. With a median blowout grain radius of 4.7 μm in our sample, spectral features are expected at $\lambda \gtrsim 30$ μm—toward the longest wavelengths covered by IRS.

4.2. MIPS Results

All sources are detected by MIPS at 24 μm and all but two have excesses at levels of 1.1–4.1 times the stellar photosphere. Twelve new MIPS 70 μm detections (C. H. Chen et al. 2009, in preparation) contribute to a total of 27 sources detected by MIPS at 70 μm, while 25 stars have 70 μm upper limits. Figure 4

[10] Hints of ∼10 μm features are seen in a few sources (for example, HD 37286, HD 74873). Chen et al. (2005) find three A stars with spectral features due to silicate grains $\lesssim$3 μm in size.

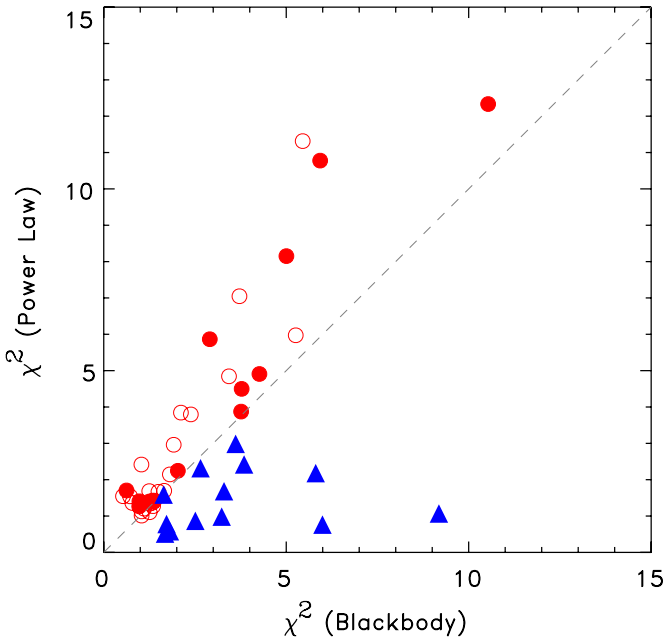

Figure 2. The χ^2 values plotted here are the best reduced χ^2 values for the 50 debris systems in our sample. The red circles are IRS sources best fit by a single-temperature blackbody, and the blue triangles are 13 disks best fit by a power law from 5 to 35 μm. The open red circles are IRS blackbody-like systems with MIPS 70 μm upper limits, while the solid symbols represent systems with MIPS 70 μm detections. Note that blackbody-like objects with or without MIPS 70 μm detections are found scattered above the diagonal, in contrast to the power-law systems where the χ^2(power law) tend to be small. Close examination of the IRS spectra shows that objects with the larger χ^2(blackbody) tend to have more warm disk structure or possibly faint features.

(A color version of this figure is available in the online journal.)

summarizes the sample distribution as a function of spectral type for the 50 objects with IRS excess, where the shaded counts are systems detected at 70 μm. All 70 μm detections are in excess of the stellar photosphere, ranging from 1.7 to 58 times the photospheric flux levels (the predicted level of photospheric emission is based on the NextGen models used in the fitting procedure described in Section 4.1.1).

Remarkably, four debris systems with excesses fit by single-temperature blackbodies are found in agreement with the 70 μm detections—narrow dust rings being the most likely grain distribution. For the majority of cases, however, when including the MIPS 70 μm photometry in the systemsÕ SEDs, the 70 μm fluxes do not agree with extrapolation of the IRS fits. The rest of the blackbody-like excesses have 70 μm detections above extrapolated values. For sources where the warm IRS excesses are best fit by a power law, the 70 μm detections are four above, three on, and six below the extrapolated power-law values. Moreover, if the MIPS 70 μm detections are added to the fitting procedure, these act as "levers"—rapidly increasing the χ^2 values and resulting in very poor fits to the short-wavelength IRS data. We thus decided to study separately the warm IRS emission, while the MIPS 70 μm detections and upper limits are added a posteriori. This approach allows us to present a uniform analysis throughout, rather than selectively use MIPS photometry only for those stars with detections, and it allows for an easier comparison with earlier IRS or MIPS-only publications. Overall, for most blackbody-like and power-law excess systems, the detected 70 μm fluxes suggest the radiation comes from an extended distribution of dust, or a distinct disk structure likely located farther out from the star than the material emitting at IRS wavelengths.

5. INTERPRETATION

As described in 4.1, we divide each IRS spectrum into two components, star and disk, where the disk emission is well fit by either a blackbody curve (with temperatures ranging from 70 to 324 K) or by a power law (with flux density slopes ranging from 1.0 to 2.9). For many systems, dust emission is also detected at 70 μm providing additional information on a possible cold disk component. Based on this information, we are able to place constraints on the physical characteristics of the disks and to look for correlations between the disk and stellar properties.

5.1. Basic Disk Properties

For an optically thin disk composed of large grains that absorb and emit as blackbodies, the disk emission can be readily translated into an underlying surface density distribution. The assumptions of optical thinness and large blackbody grains ($2\pi a_{\rm grain} > \lambda$) are justified by the overall fractional luminosities and the lack of spectral features (plus the relatively large blowout size for dust around A stars). Depending on their size and composition, grains may depart from blackbody behavior, but we set aside this possibility in the following discussion. Large grains located at a single radial location (or narrowly confined) will produce a single temperature blackbody component. A disk with a power-law flux distribution, meanwhile, corresponds to a disk with a power-law density distribution. A full derivation of this relationship is presented in Appendix A; for illustrative purposes we show here using dimensional arguments how a given spectral flux slope can be related to the radial optical depth distribution.

The flux contributed by a single annulus of the disk with width ΔR goes as

$$\Delta F \propto \tau \sigma T_{\rm dust}^4 2\pi R \Delta R, \quad (4)$$

where τ is the effective (or perpendicular) optical depth at radius R. While a power-law flux distribution corresponds to a superposition of many blackbodies, the flux from dust at a given temperature can be approximated as emission at a characteristic wavelength with $\lambda \propto T_{\rm dust}^{-1}$ (Wien's Law). The dust temperature is set by the illumination from the central star, such that $T_{\rm dust}^4 \propto R^{-2}$ and so, $R \propto \lambda^2$.

Substituting these simple relationships among λ, R, and $T_{\rm dust}$ into Equation (4), we get

$$\Delta F \propto \tau \Delta\lambda/\lambda. \quad (5)$$

In order to compare to the slope of the flux density ($F_\nu \equiv \Delta F/\Delta\nu$), we then include $\Delta\nu = c\Delta\lambda/\lambda^2$, getting simply $F_\nu \propto \tau\lambda$. Given a flux distribution $F_\nu \propto \lambda^\alpha$, the disk's effective optical depth is then

$$\tau \propto F_\nu/\lambda \propto \lambda^{\alpha-1} \propto R^{(\alpha-1)/2}. \quad (6)$$

Note that a constant optical depth disk, as expected for a disk dominated by Poynting–Robertson (P–R) drag, will have a flux distribution with slope $\alpha = 1$ (Wyatt et al. 2005). A flux slope $\alpha = 3$, meanwhile, corresponds to a disk with optical depth $\propto R$. The observed flux slopes range from $\alpha = 1.0$ to 2.9, corresponding to effective optical depth

Table 3
Dust Properties from Excess

HD Name	$T_{\rm dust}$ (K)	$D_{\rm dust}$ (AU)	$a_{\rm BOS}$[a] (μm)	$F_{\nu,24}$[b] (mJy)	$F_{\nu,70}$[b] (mJy)	$L_{\rm dust,IRS}/L_\star$	$L_{\rm dust,MIPS70}/L_\star$	$M_{\rm dust,BB,IRS}$ ($M_\leftmoon$)	$M_{\rm dust,BB,70um}$ ($M_\leftmoon$)	$T_{\rm PR}/T_{\rm COLL}$	
001404	184	12	4.7	155.1 ± 1.2	58.7 ± 4.39	1.2E-05	4.1E-06	1.2E-04	6.8E-03	5.1	...
023267	180	16	6.2	36.0 ± 0.4	16.31 ± 2.31	9.9E-05	...	2.5E-03	...	47.9	...
023642	101	52	6.2	17.7 ± 2.2	47.7 ± 24.5[c]	1.7E-05	8.9E-05[c]	4.2E-03	...	14.3	...
023763	70	93	4.3	17.7 ± 2.2	47.1 ± 14.3[c]	1.1E-05	5.5E-05[c]	6.1E-03	...	12.7	...
024141	215	6	2.3	65.9 ± 1.2	12.6 ± 12.6[c]	1.9E-05	1.0E-05[c]	2.1E-05	...	6.3	...
024817	276	5	4.7	45.1 ± 0.4	6.3 ± 42.7[c]	3.5E-05	4.6E-05[c]	6.9E-05	...	10.1	...
028355	113	18	1.9	138.8 ± 1.4	178.21 ± 15.68	1.8E-05	1.6E-05	1.7E-04	3.6E-03	11.6	...
032977	187	8	2.3	95.7 ± 0.8	7.8 ± 28.6[c]	2.0E-05	1.4E-05[c]	4.0E-05	...	7.7	...
037286	186	11	4.7	65.2 ± 1.3	38.4 ± 13.1[c]	5.7E-05	2.7E-05[c]	5.3E-04	...	24.3	...
074873	189	13	4.3	66.8 ± 0.7	22.7 ± 5.8[c]	3.3E-05	9.6E-06[c]	3.6E-04	...	14.6	...
080950	187	15	6.2	117.4 ± 1.4	61.46 ± 2.10	1.2E-04	...	2.5E-03	...	53.9	...
087696	182	7	1.9	214.3 ± 2.8	41.43 ± 7.30	1.3E-05	...	1.8E-05	...	5.1	...
092536	251	14	15.8	46.8 ± 0.9	0.1 ± 21.7[c]	1.0E-04	4.2E-05[c]	5.1E-03	...	40.3	...
093738	265	8	8.3	24.3 ± 1.3	20.3 ± 7.8[c]	2.9E-05	2.6E-05[c]	2.6E-04	...	9.8	...
098673	192	6	1.9	43.1 ± 0.8	36.62 ± 3.93	3.0E-05	1.4E-05	3.3E-05	3.1E-03	11.0	...
115892	190	11	4.7	699.4 ± 0.4	105.16 ± 12.87	1.4E-05	...	1.2E-04	...	5.7	...
125283	194	11	4.7	46.2 ± 1.2	−5.5 ± 11.8[c]	1.6E-05	7.9E-06[c]	1.3E-04	...	6.7	...
126135	209	21	15.8	22.9 ± 2.0	13.4 ± 5.5[c]	7.3E-05	3.5E-05[c]	7.5E-03	...	34.4	...
128207	193	24	15.8	31.5 ± 0.7	9.2 ± 5.2[c]	1.2E-05	8.8E-06[c]	1.6E-03	...	5.9	...
132238	240	16	15.8	31.6 ± 0.8	−1.3 ± 6.8[c]	6.9E-05	1.4E-05[c]	4.1E-03	...	28.3	...
135379	171	12	3.0	336.5 ± 3.1	75.5 ± 84.2[c]	2.6E-05	1.6E-05[c]	1.7E-04	...	11.9	...
135454	324	7	9.5	18.1 ± 0.2	−8.0 ± 4.3[c]	3.5E-05	3.2E-06[c]	2.3E-04	...	10.0	...
136246	158	18	4.3	15.0 ± 0.4	36.76 ± 4.78	1.5E-05	3.2E-05	3.3E-04	6.4E-02	7.9	...
136482	208	18	12.3	42.4 ± 0.0	25.06 ± 2.57	1.1E-04	2.0E-05	7.3E-03	3.4E-01	51.6	...
137015	224	8	4.7	15.6 ± 0.1	−13.4 ± 11.5[c]	1.4E-05	1.6E-05[c]	6.3E-05	...	4.9	...
138923	286	11	15.8	57.7 ± 0.4	3.5 ± 9.6[c]	1.5E-04	1.9E-05[c]	4.5E-03	...	52.7	...
142139	176	11	3.0	60.5 ± 1.5	46.5 ± 18.2[c]	1.5E-05	2.6E-05[c]	8.3E-05	...	6.4	...
145964	98	73	9.5	19.5 ± 1.9	10.2 ± 6.1[c]	8.1E-06	1.6E-05[c]	6.2E-03	...	7.6	...
159170	209	6	2.3	85.7 ± 1.9	17.5 ± 9.7[c]	2.3E-05	7.6E-06[c]	3.0E-05	...	8.2	...
159492	160	10	2.3	196.7 ± 2.4	170.83 ± 10.59	4.5E-05	2.0E-05	1.7E-04	7.1E-03	20.5	...
182919	206	13	6.2	62.3 ± 0.8	20.1 ± 20.4[c]	3.2E-05	2.2E-05[c]	4.8E-04	...	13.6	...
183324	126	34	6.2	51.2 ± 1.5	29.97 ± 5.59	1.3E-05	6.3E-06	1.3E-03	2.4E-02	8.6	...
191174	259	6	3.2	39.5 ± 2.0	32.52 ± 11.32	5.2E-05	1.5E-05	8.4E-05	1.6E-02	16.3	...
192425	185	12	4.7	132.4 ± 1.4	164.91 ± 11.09	2.8E-05	2.0E-05	2.7E-04	3.3E-02	11.9	...
215766	186	20	9.5	63.3 ± 1.1	36.7 ± 8.9[c]	3.9E-05	1.9E-05[c]	2.3E-03	...	19.2	...
220825	204	13	6.2	110.9 ± 0.9	26.2 ± 7.2[c]	2.9E-05	6.5E-06[c]	4.5E-04	...	12.3	...
223325	191	15	6.2	163.0 ± 1.6	59.14 ± 6.31	2.3E-05	5.1E-06	4.6E-04	2.0E-02	10.4	...

HD Name	Slope α		$a_{\rm BOS}$[a] (μm)	$F_{\nu,24}$[b] (mJy)	$F_{\nu,70}$[b] (mJy)	$L_{\rm dust,IRS}/L_\star$	$L_{\rm dust,MIPS70}/L_\star$	$M_{\rm dust,PL,IRS}$ ($M_\leftmoon$)	$M_{\rm dust,BB,70um}$ ($M_\leftmoon$)	$T_{\rm PR}/T_{\rm COLL}$ $D_{35\,\mu\rm m}$	$D_{10\,\mu\rm m}$
010939	1.9	...	4.3	103.5 ± 2.1	384.62 ± 16.52	3.3E-05	5.8E-05	1.7E-03	1.2E-01	3.3	0.3
030422	1.4	...	3.0	44.7 ± 1.2	67.31 ± 1.18	2.7E-05	2.0E-05	7.0E-04	1.6E-02	2.8	0.5
038056	1.2	...	6.2	36.3 ± 1.0	50.21 ± 6.65	7.2E-05	3.0E-05	3.7E-03	1.2E-01	3.3	0.7
038206	1.1	...	6.2	107.7 ± 3.3	377.41 ± 14.19	1.9E-04	1.4E-04	6.4E-03	5.3E-01	5.5	1.4
070313	1.6	...	3.0	81.5 ± 1.9	223.88 ± 8.80	4.0E-05	4.6E-05	8.7E-04	3.6E-02	3.7	0.5
071722	1.9	...	6.2	55.8 ± 1.3	155.13 ± 3.62	6.1E-05	5.9E-05	3.8E-03	2.3E-01	3.9	0.4
079108	1.2	...	6.2	45.9 ± 1.3	83.25 ± 9.78	6.6E-05	3.6E-05	3.3E-03	1.4E-01	2.9	0.7
110411	2.0	...	6.2	140.7 ± 3.3	242.79 ± 9.32	3.5E-05	2.8E-05	2.9E-03	1.1E-01	3.1	0.2
138965	2.4	...	4.3	69.4 ± 5.6	562.51 ± 15.90	1.5E-04	3.1E-04	4.2E-03	6.2E-01	8.6	0.4
141378	2.2	...	2.3	74.4 ± 1.8	232.85 ± 39.07	2.7E-05	4.6E-05	4.1E-04	1.6E-02	4.1	0.3
153053	2.9	...	2.3	78.8 ± 1.2	168.91 ± 9.06	1.6E-05	2.6E-05	3.2E-04	9.2E-03	3.6	0.1
196544	1.3	...	4.7	75.7 ± 1.3	74.04 ± 9.38	3.8E-05	1.5E-05	1.5E-03	2.5E-02	2.9	0.6
225200	1.0	...	6.2	34.9 ± 0.9	99.12 ± 1.84	4.9E-05	4.8E-05	2.8E-03	1.9E-01	2.3	0.6

Notes.
[a] Blowout size.
[b] Measured MIPS photometry, not color corrected.
[c] Upper limit.

distributions ranging from constant throughout to increasing linearly with radius. Based on this calculation, we assume here that a power law going from λ_1 to λ_2 is a power-law dust distribution over radii for which emission peaks at these two wavelengths.

5.1.1. Fractional Dust Luminosity

The disk fractional luminosity, $L_{\rm dust}/L_\star$, can be measured directly from the observed SED. This is a primary disk parameter in that it is an indicator of the total grain surface area that

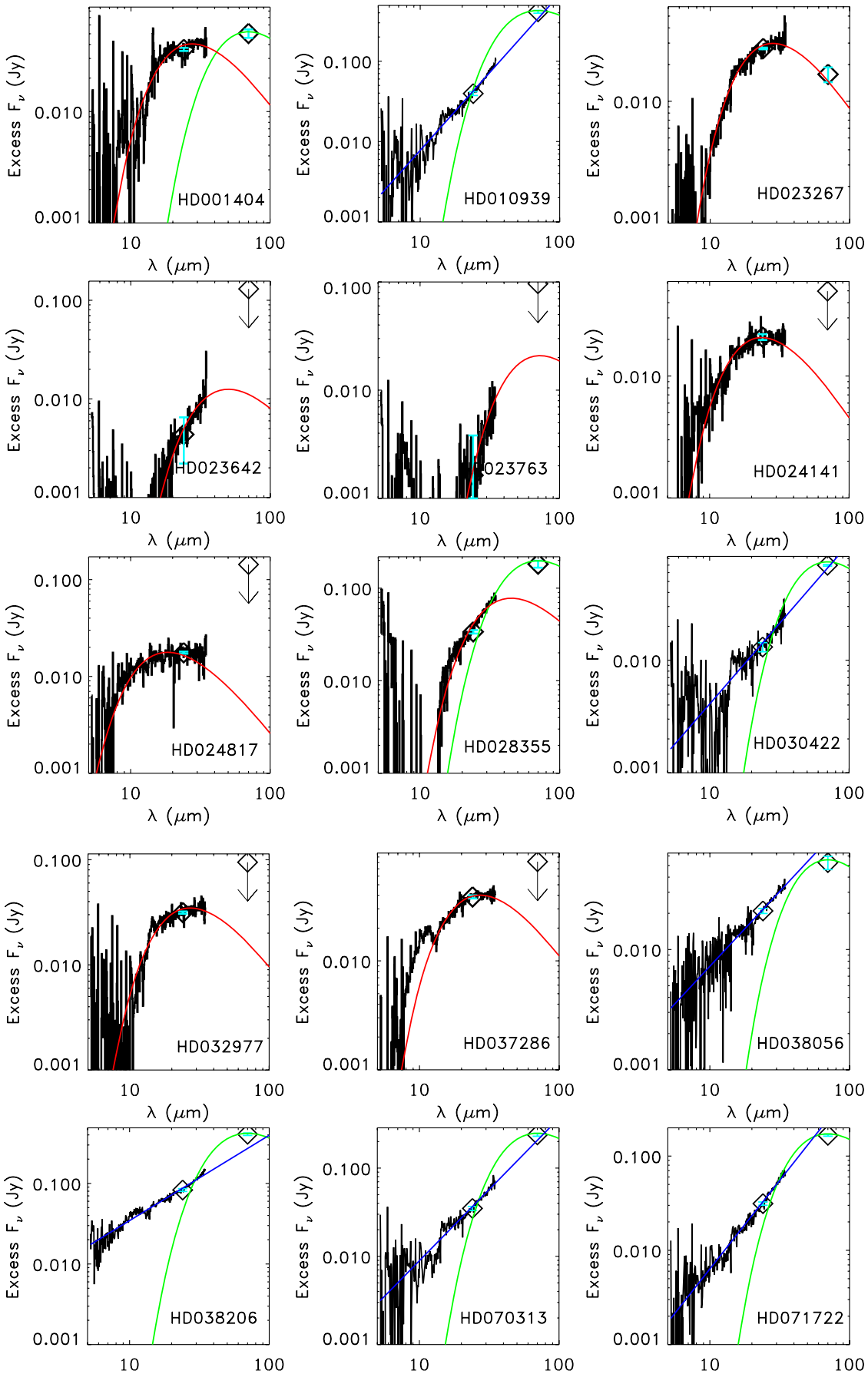

Figure 3. Photosphere-subtracted IRS spectra and MIPS 24 and 70 μm residual fluxes (black diamonds) plotted with F_ν as a function of wavelength. The reduced χ^2 fits for single-temperature blackbody and power-law models are overplotted in red and blue, respectively, along with a green blackbody curve peaking at the MIPS 70 μm point ($T_{70\,\mu\mathrm{m}} \approx 52$ K) for visual aid. The black diamonds with down arrows are MIPS 70 μm upper limits.

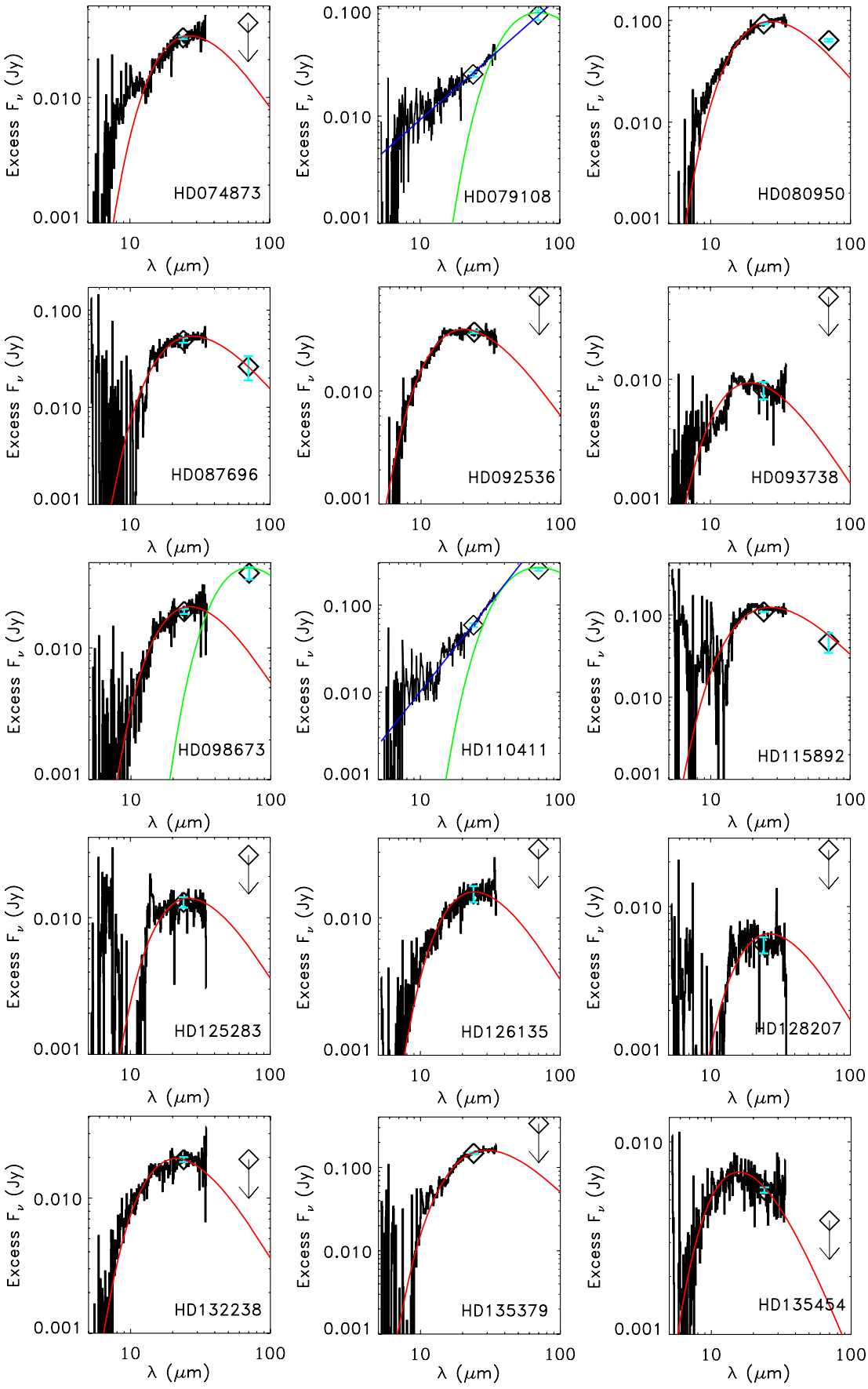

Figure 3. (Continued)

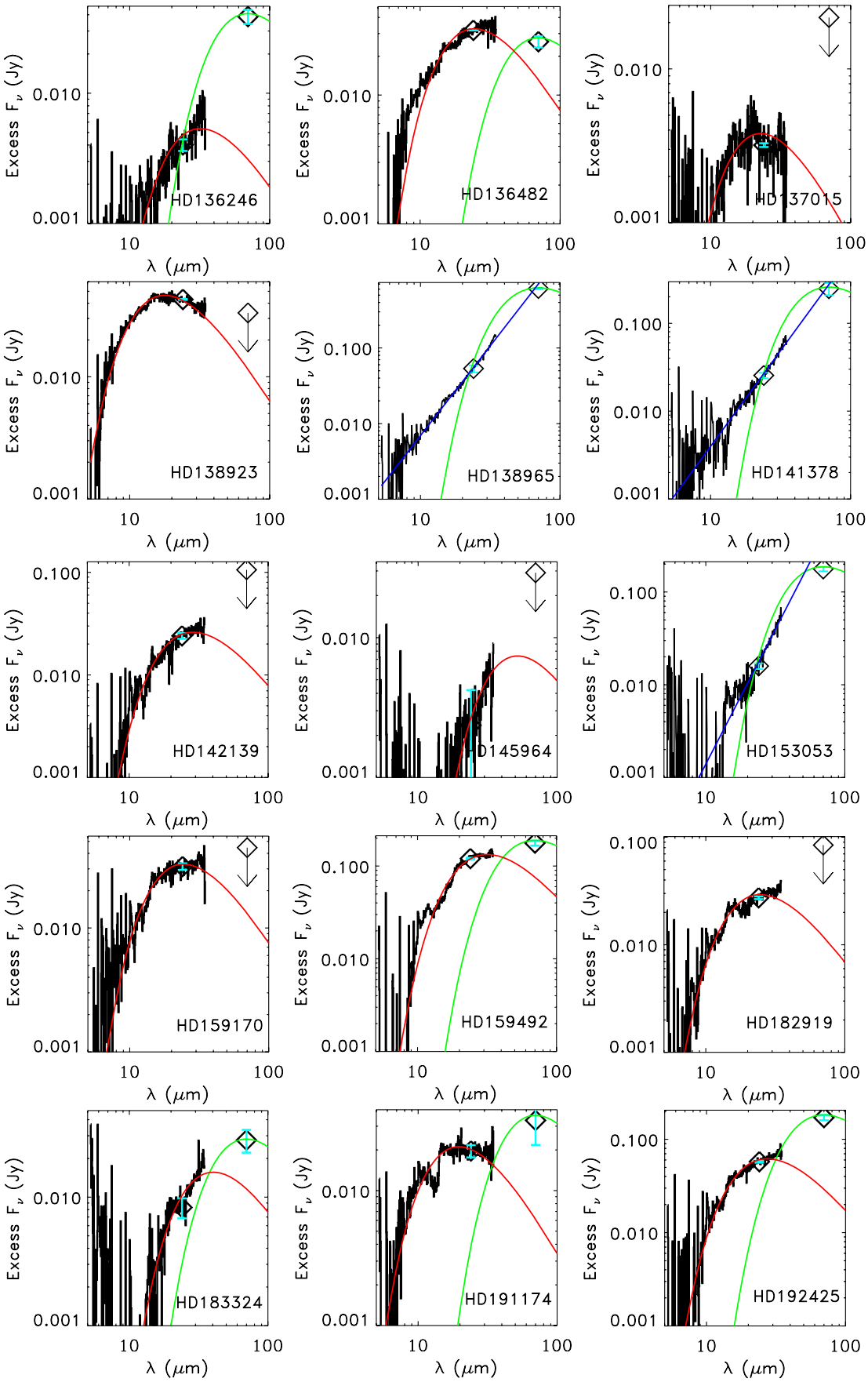

Figure 3. (Continued)

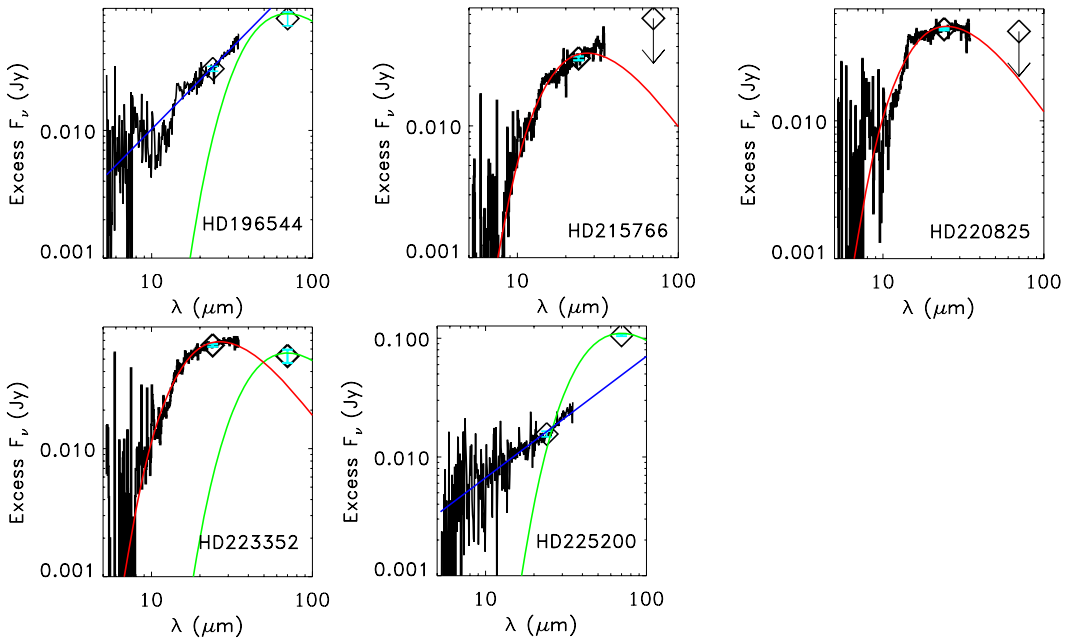

Figure 3. (Continued)

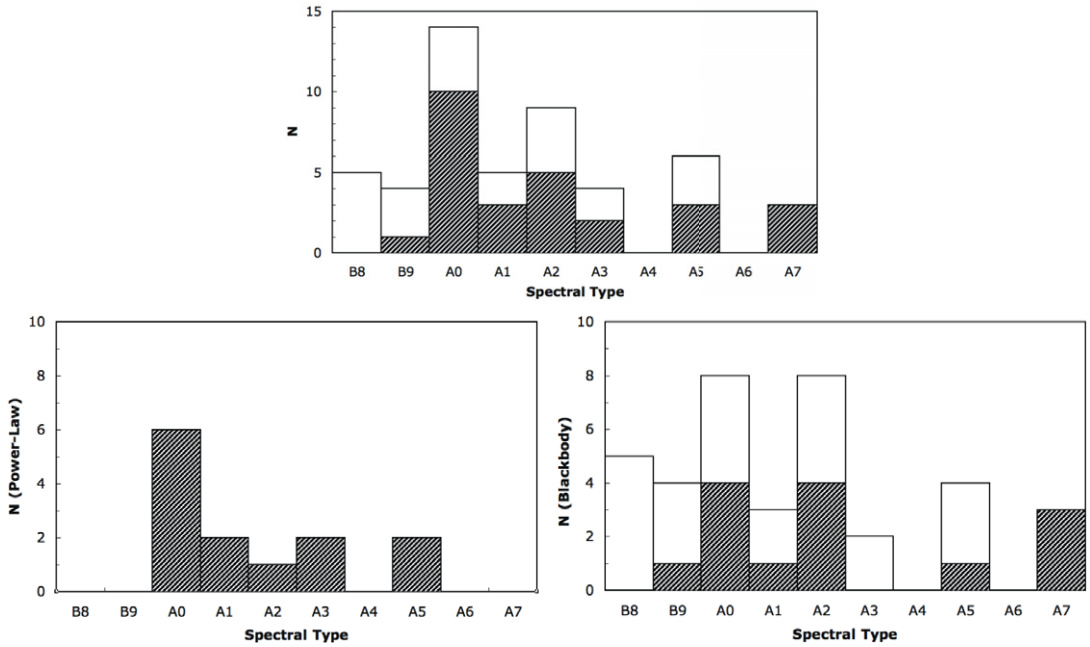

Figure 4. Top: number counts vs. spectral type for the 50 sources with IRS excess in our sample (HD 136347 and HD 166046 have been left out since no excess emission was detected with *Spitzer's* IRS nor MIPS wavelengths). Bottom left are the number counts for stars with power-law excess disks, and bottom right are counts for sources with blackbody-like excess emission at the IRS wavelengths. The shaded gray counts are sources detected with *Spitzer* MIPS 70 μm; the rest have 70 μm upper limits. Note the 13 sources where excess emission is best fit by a power-law disk model at the IRS wavelengths are all detected at 70 μm.

is reprocessing stellar light. Though the dust emission is not known at very long wavelengths (corresponding to very cold temperatures), the mid-IR SED strongly constrains the emission from warm dust. We first calculate the fractional excess luminosity based on the IRS data only. We add up all the flux observed at the IRS wavelengths (5.3–35 μm) and then assume that the radiation falls off as a blackbody longward of 35 μm–for sources best fit by a blackbody we extrapolate the blackbody fit, and for sources with power-law SEDs we use a blackbody that peaks at 35 μm ($T = 105$ K). Independent of the thermal fit, our extrapolations go out to 50 μm only. Listed in Table 3, the minimum values of $L_{\rm dust,IRS}/L_\star$ for the blackbody-fit disks range between 8.1×10^{-6} and 1.5×10^{-4}, and for power-law excess disks we find $L_{\rm dust,IRS}/L_\star$ lower limits between 1.6×10^{-5} and 1.9×10^{-4} (note $L_{\rm dust,IRS}/L_\star$ are dust fractional luminosities shortward of 50 μm).

Next, we consider the 70 μm photometry and estimate a minimum $L_{\rm dust,MIPS70}/L_\star$ associated with the 70 μm emission (for sources where 70 μm detections are in excess of the IRS fits). Although the MIPS 70 μm data points are very reliable measurements of circumstellar dust, it is not clear from the 70 μm flux only where the bulk of the colder-than-IRS-emitting material is located. For a minimum estimate, we assume that the far-IR emission comes from a population of cold blackbody grains whose energy flux (νF_ν) peaks at the MIPS 70 μm effective wavelength of 71.4 μm. This corresponds to a dust

temperature of 51.5 K. Values of $L_{\rm dust,MIPS70}/L_\star$ are listed in Table 3, and account for the minimum excess energy seen longward of 50 μm. Note that we have calculated values of $L_{\rm dust}/L_\star$ for the IRS and MIPS measurements independently of each other. Both are intended to be minimum values based on each set of data.

The $L_{\rm dust,MIPS70}/L_\star$ lower limits range from 4.1×10^{-6} to 3.1×10^{-4} for 23 systems (13 power-law systems and 10 blackbody-like where the flux at 70 μm is in excess of the extrapolated 70 μm value based on the warmer IRS blackbody component). Figure 5 shows that the 70 μm and IRS emission correlate for detected sources. Our calculation implicitly makes the assumption that the IRS and MIPS 70 μm emission probes two disk structures. Assuming that the minimum dust luminosities are not too far from the true dust luminosities, the results show that over our sample, the two structures can absorb similar fractions of the stellar luminosity. In general, the short wavelength luminosity is stronger; yet, for a few stars, the 70 μm luminosity exceeds that of shorter wavelength by up to $\sim$2×. The minimum $L_{\rm dust,MIPS70}/L_\star$ observed in our sample are high compared to the $\sim 10^{-7}$–10^{-6} inferred for the Kuiper Belt (Backman et al. 1995; Fixsen & Dwek 2002), suggesting the presence of more dusty debris than in our present day solar system.

5.1.2. Dust Mass

While a disk's fractional luminosity can be readily measured from its SED, the dust mass can be only indirectly estimated. A minimum dust mass, $M_{\rm dust,BB}$, can be calculated by assuming the grains are as small as possible without being blown out from the system. We set the dust radius equal to $a_{\rm BOS}$ (calculated from Equation (3) above and listed in Table 3). We assume an average grain material density of $\rho_g = 3$ g cm^{-3} for typical silicate dust. In order to calculate the total dust absorbing area intersecting starlight, we must first estimate its orbital location. This distance, R, can be inferred from the observed dust temperatures (Table 3). For large blackbody grains of unit emissivity and temperature $T_{\rm dust}$, the distance is

$$R = \frac{1}{2}\left(\frac{T_\star}{T_{\rm dust}}\right)^2 R_\star, \quad (7)$$

where $T_\star$ is the effective temperature of the stellar photosphere, and $R_\star$ is the stellar radius (Jura et al. 1998). The distances inferred from the IRS spectral fits of single-temperature blackbodies are between 5.2 and 93.3 AU, with a median distance of 11.9 AU (Table 2). Using the grain's orbital distances and the minimum blowout sizes (also in Table 2), a system's minimum dust mass is given by (Jura et al. 1995)

$$M_{\rm dust,BB} = \frac{16\pi}{3}\frac{L_{\rm dust}}{L_\star}\rho_g a_{\rm BOS} R^2. \quad (8)$$

The 37 systems with single-temperature blackbody fits at the IRS wavelengths yield minimum dust masses $M_{\rm dust,BB,IRS}$ ranging between 1.8×10^{-5} $M_\leftmoon$ (lunar masses) for HD 87696, and 7.5×10^{-3} $M_\leftmoon$ for HD 126135. The four objects with 70 μm detections agreeing with the short wavelength blackbody fit have minimum warm dust masses between 1.3×10^{-5} $M_\leftmoon$ and 1.2×10^{-4} $M_\leftmoon$. Ten blackbody-like cases show a surplus of MIPS 70 μm flux in excess of the warmer IRS blackbody fit component. While the IRS spectra provide a clear measurement of dust temperature, the MIPS photometry does not well constrain the temperature of the colder dust responsible for the 70 μm emission. Assuming dust material at a temperature corresponding to 70 μm emission ($T = 51.5K$), the resulting nominal dust masses inferred from the MIPS 70 μm photometry are $0.003\ M_\leftmoon < M_{\rm dust,BB,70um} < 0.34\ M_\leftmoon$, considerably larger than the estimates for the dominant disk component at the IRS wavelengths.

We can estimate a minimum dust mass, $M_{\rm dust,PL,IRS}$ for the 13 sources best fit by a power-law flux distribution using the power-law slope, α, by

$$M_{\rm dust,PL,IRS} > 2 \times 10^{-6}\ M_\oplus \left(\frac{10^{(\alpha-1)/2}}{\alpha+3}\right)\left(\frac{\tau_0}{10^{-5}}\right) \times \left(\frac{a_{\rm BOS}}{10\,\mu{\rm m}}\right)\left(\frac{\rho_g}{3\,{\rm g\,cm^{-3}}}\right)\left(\frac{L_\star}{L_\odot}\right)^{(\alpha+3)/4}, \quad (9)$$

where τ_0 (a function of α and the overall magnitude of dust emission at 24 μm), is the extrapolated optical depth of the disk at 1 AU from the central star (see Appendix A for a full derivation). We find the 13 systems that are power laws at IRS wavelengths to have warm disk components of minimum dust masses ranging between 3.2×10^{-4} $M_\leftmoon$ and 6.4×10^{-3} $M_\leftmoon$. To estimate the amount of material emitting at 70 μm, we again use Equation (8), and a distance corresponding to 51.5 K. We find $0.009\ M_\leftmoon < M_{\rm dust,BB,70um} < 0.62\ M_\leftmoon$ in addition to the warm material estimated from the power laws at IRS. The power-law debris disk HD 138965 yields the largest dust mass lower limit of 0.62 $M_\leftmoon$. Figure 6 shows the minimum inferred dust masses from the MIPS 70 μm and IRS detections. Overall, power-law debris disks not only tend to be a bit more luminous (Figure 5) than debris emitting as blackbodies at IRS, they are also more massive (Figure 6). In general, there is a couple of orders of magnitude more mass at distances probed by MIPS 70 μm than the mass estimated from IRS only.

Our methods to estimate dust masses above are a conservative approach since we assume grains with radii set by the radiative blowout limit ($a_{\rm BOS}$) for both IRS and MIPS 70 μm calculations (including albedo and emissivity effects will only increase the mass estimates). A large amount of mass in the form of larger grains, pebbles, rocks, etc., may exist in these systems but evade detection due to a low surface area to mass ratio. The size of the parent bodies whose collisions produce the observed dust is very uncertain, but simulations of debris disk evolution around A stars suggest that kilometer-sized bodies are required in order to fit the observations of disk brightness evolution (Wyatt et al. 2007). Assuming a standard collisional cascade slope for the size distribution (−3.5; Dohnanyi 1968), the mass contained in parent bodies is equal to $M_{\rm min\ dust} \times \sqrt{a_{\rm max}/a_{\rm min}}$. So for a planetesimal size of 1 km and minimum dust size of $\sim 10\,\mu$m, the total system mass is a factor of 10^4 greater than the conservative dust masses estimated above, upward of $\sim$76 $M_\oplus$ in some cases.

5.2. Correlations

An advantage of investigating debris disks around A stars is that their ages can be estimated from simple arguments, allowing for an examination of the temporal evolution of disks. For the 45 debris disk systems with assigned ages (Table 1), we consider how the disk properties (dust temperature, power-law slope, and fractional dust luminosity; see Table 3) vary with stellar age. Figure 7 shows the evolution of the dust emission temperature at the IRS wavelengths. There is a larger scatter of $T_{\rm dust}$ among the younger systems, but the median grain temperature of 190 K

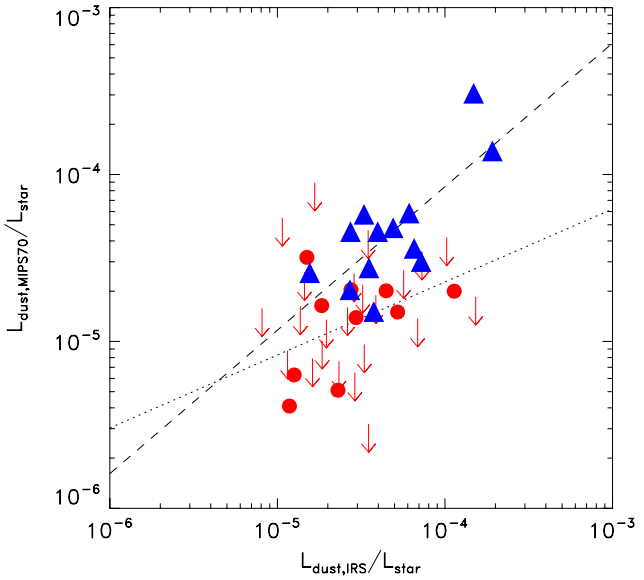

Figure 5. Minimum dust luminosity ratios from MIPS (70 μm) and IRS. The minimum luminosity ratios are extrapolated out to 50 μm for the warm IRS-measured components, and longward of 50 μm for the MIPS 70 μm contribution. The red circles are systems well modeled by a single-temperature blackbody at IRS wavelengths that have been detected at 70 μm, and where the 70 μm measurement is in excess of the extrapolated IRS fit. The blue triangles are debris exhibiting power-law excess flux distributions at IRS wavelengths (all detected at 70 μm). The down arrows represent sources best fit by a blackbody at IRS but with upper limits at 70 μm. The dotted and dashed lines are linear fits through the blackbody and power-law populations, respectively. The minimum stellar luminosity reradiated shortward of 50 μm is generally greater than the minimum reradiated longward of 50 μm.

(A color version of this figure is available in the online journal.)

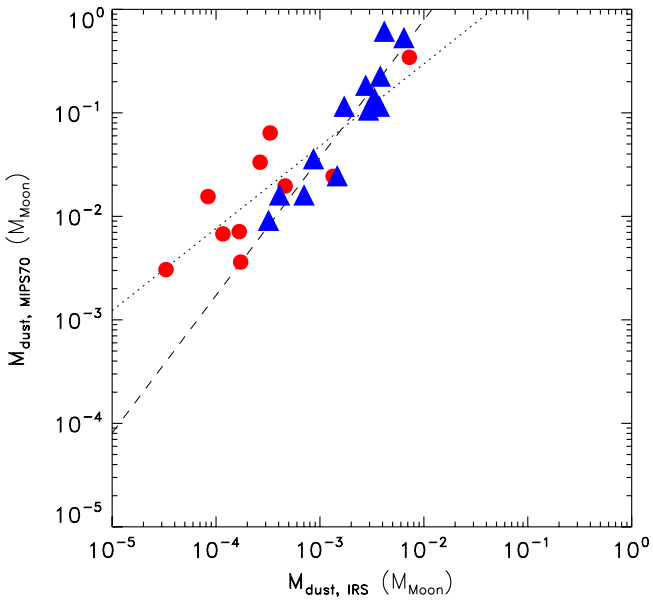

Figure 6. Nominal dust mass inferred assuming cold 70 μm emitting material vs. minimum warm dust mass seen with IRS for 23 sources with MIPS 70 μm surplus in excess (Four blackbody-like sources have 70 μm emission in close agreement with the IRS blackbody fit, and are thus not included in this plot). The red circles are blackbody-fit excess systems, and the blue triangles are debris disks seen as power laws at IRS wavelengths. As expected, systems with power-law excesses tend to be more massive than the blackbody population. A two-dimensional Kolmogorov–Smirnov (K–S) statistical test shows power-law debris disks differ significantly (>98%) from the blackbody population. The dotted and dashed lines are line fits through each population—blackbody and power law, respectively—to show power laws (with dashed line) have a tighter correlation to their 70 μm counterpart. If large 70 μm emitting grains are located in colder outer regions, the mass implied by the 70 μm flux is ~1–2 orders of magnitude greater than that required to produce the flux seen at the shorter IRS wavelengths.

(A color version of this figure is available in the online journal.)

is more or less constant throughout the age range covered by our sample. For the excess spectra that better follow power laws, the dust cannot be characterized by a single dust temperature. For these systems we instead plot the slope of the excess flux, α, against age (Figure 8). While the source with the largest slope of 2.9 is also the oldest (HD 153053) there is no clear trend in slope evolution among the group as a whole. However, with larger samples of A stars, it has been shown that the excesses at 24 μm decay more quickly than those at 70 μm (Su et al. 2006).

While all debris systems—blackbody and power law—are more common around younger stars, all of the observed systems are old enough to have cleared their primordial material. The blowout timescales are typically ~10–100 times smaller than the lifetimes for grain destruction mechanisms like P–R drag or collisional grinding, which in turn are much smaller than the ages of the youngest star in our sample.

We estimate a minimum dust fractional luminosity ($L_{dust}/L_{\star}$), where $L_{dust}/L_{\star} = L_{dust,IRS}/L_{\star} + L_{dust,MIPS70}/L_{\star}$, using the known information of a system's SED by integrating the energy under the IRS data points plus the contribution of a cold blackbody peaking at 70 μm. In Figure 9, we plot our fractional luminosity values and upper limits as a function of age. Our results are consistent with previous findings by Rieke et al. (2005); Su et al. (2006) that most systems with dust luminosity ratio in the range 10^{-4}–10^{-3} are young, and debris systems have an overall decrease in $L_{dust}/L_{\star}$ with time.

We next consider disk property dependence on spectral type. Figure 4 shows the number of systems versus stellar spectral type for the 50 sources with IRS excesses (top panel), for systems with power-law excess flux distributions (lower left), and for stars with excesses modeled by single-temperature blackbody distributions (lower right). The systems with 70 μm detections are indicated by the shaded regions in each panel, and show no spectral type dependence. We also found no discernible trend of T_{dust} or slope (α) with spectral type. Although our sample covers a spectral range from B8 to A7, over half our sources are found between A0 and A2. The trend of properties with spectral type has been explored better with samples that have a large range, e.g., Trilling et al. (2008).

The strength of the far-IR emission, however, has a striking correlation with the shape of the IRS mid-IR emission. Note that all 13 stars with power-law excess flux are detected at 70 μm (the entire histogram is filled in the lower left panel of Figure 4). This may be what is to be expected to first order as the 13 power-law spectra are all rising to longer wavelengths, but it underscores the difference between the blackbody and power-law thermal profiles. The correlation between IRS power-law excess and 70 μm emission is in strong contrast to the remaining debris systems with blackbody-like IRS emission (lower right panel in Figure 4) where less than half (14/37) have MIPS 70 μm detections at greater than 3σ level.

5.3. Radiation- Versus Collision-Dominated Disks

Dust in a low-density debris disk environment is subject to mechanisms that will destroy grains and remove them from the system. Grains smaller than the blowout limit are quickly ejected by stellar photon pressure. Grains not blown out by the central star will spiral inward due to radiation-induced P–R drag, which can remove dust on timescales much shorter than the lifetime

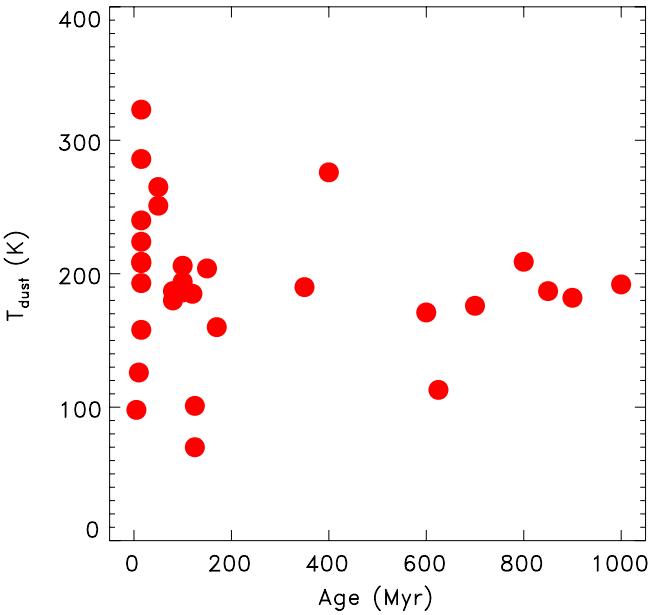

Figure 7. Inferred dust temperature vs. age for 33 blackbody-like excess systems with estimated stellar ages. Although most debris systems are younger than 200 Myr, the mean T_{dust} value of 190 K is predominant throughout the age range studied in this sample.

(A color version of this figure is available in the online journal.)

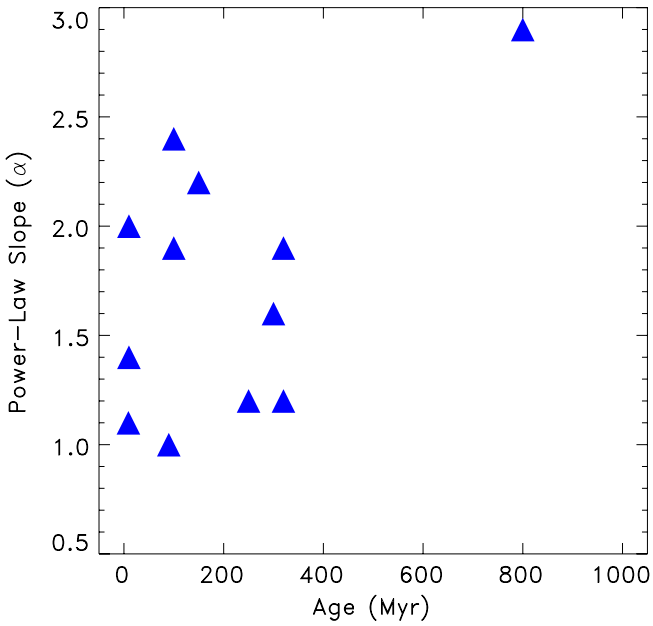

Figure 8. Slope of power-law SEDs vs. age. Twelve debris disks with age estimates are shown. Most power-law excess systems are younger than 400 Myr, while the oldest is also the one showing the steepest slope.

(A color version of this figure is available in the online journal.)

of the system—∼1000 years for micron-sized grains at 1 AU in the solar system (Gustafson 1994). More generally, the time for dust to spiral into the central star under the action of P–R drag can be written as

$$T_{\rm PR} = 8 \times 10^4 \,{\rm yr} \left(\frac{R}{10\,{\rm AU}}\right)^2 \left(\frac{M_\star}{M_\odot}\right)^{-1} \left(\frac{a}{a_{\rm BOS}}\right) \quad (10)$$

(note that we have defined $T_{\rm PR}$ in terms of the $a_{\rm BOS}$ which in turn depends on the star's luminosity). A steady supply of material moving inward by P–R drag (with no other forces) will result in a continuous disk of uniform surface density (Wyatt 2005), corresponding to a spectral flux distribution with slope $\alpha = 1$ (see Equation (6) and Appendix A).

Dust also loses angular momentum to stellar wind drag at a rate dependent on the star's mass-loss rate (e.g., Minato et al. 2006). A-type stars do not have strong stellar winds relative to their luminosity, so that stellar wind drag is generally much less effective than P–R drag and does not contribute much toward dust removal around stars in our sample.

Of much greater importance, dust particles will collide with each another in regions where the particle density is high. These collisions can act as an effective dust removal mechanism, with the resulting small fragments quickly blown out of the system by radiation pressure. The average time for the smallest grains to collide with each other is a simple function of the disk's effective (or perpendicular) optical depth, τ, and the local orbital period, $T_{\rm orbit}$:

$$T_{\rm COLL} = \frac{T_{\rm orbit}}{4\pi\tau} = 2.5 \times 10^5 \,{\rm yr} \left(\frac{R}{10\,{\rm AU}}\right)^{3/2} \left(\frac{M_\star}{M_\odot}\right)^{-1/2} \left(\frac{\tau}{10^{-5}}\right)^{-1} \quad (11)$$

(Backman & Paresce 1993; Wyatt et al. 1999). In calculating τ for blackbody-like IRS-detected debris we take the width of a ring $\Delta R = 0.1R$. Note that grain lifetimes $T_{\rm PR}$ and $T_{\rm COLL}$ above apply to grains in the vicinity of $a_{\rm BOS}$.

The relative importance of collisional and P–R drag grain removal depends on the location in the disk. Our systems best fit by a blackbody model at IRS wavelengths have dust collisional lifetimes considerably shorter than the P–R drag lifetimes. For the power-law disks, which extend over a range of orbital radii, we have calculated $T_{\rm PR}$ and $T_{\rm COLL}$ at two radii—the locations corresponding to dust whose emission peaks at 10 or at 35 μm. At the outer IRS disk (35 μm), all of the systems are dominated by collisional destruction ($T_{\rm PR} > T_{\rm COLL}$). However, for distances corresponding to ∼10 μm emission in power-law systems, P–R drag removes dust more rapidly than collisions ($T_{\rm PR} < T_{\rm COLL}$) as they fall below the diagonal in Figure 10. The ratio of the timescales, $T_{\rm PR}/T_{\rm COLL}$, is listed for each system in Table 3.

While previous work has emphasized the importance of collisional processes relative to P–R drag (Dominik & Decin 2003; Wyatt 2005), it is worth noting that the dominance of collisions holds only for the densest (and hence most easily observed) parts of the disk. Systems with blackbody-like excesses, although $T_{\rm PR}/T_{\rm COLL}$ may be $\gg 1$, will probably have more tenuous interior regions in which P–R drag becomes increasingly important. For the power-law systems observed in our survey, the transition region appears to be close to or straddled by the IRS observations; the median timescale ratios ($T_{\rm PR}/T_{\rm COLL}$) are ∼6 and < 1 at distances corresponding to 35 μm and 10 μm emission, respectively.

5.4. Inner/Warm IRS Versus Outer/Cold MIPS Components

Observations of debris systems with *Spitzer*'s IRS and with MIPS 70 μm can provide information about distinct spatial regions and of grains under very different physical conditions. Figure 11 (top) shows a dust distance histogram for 37 sources where the IRS excess emission is better modeled by a single-temperature blackbody. The radial location of dust is inferred from the best-fit dust temperature, $T_{\rm dust}$, assuming large blackbody grains to be in thermal equilibrium with the star. Also

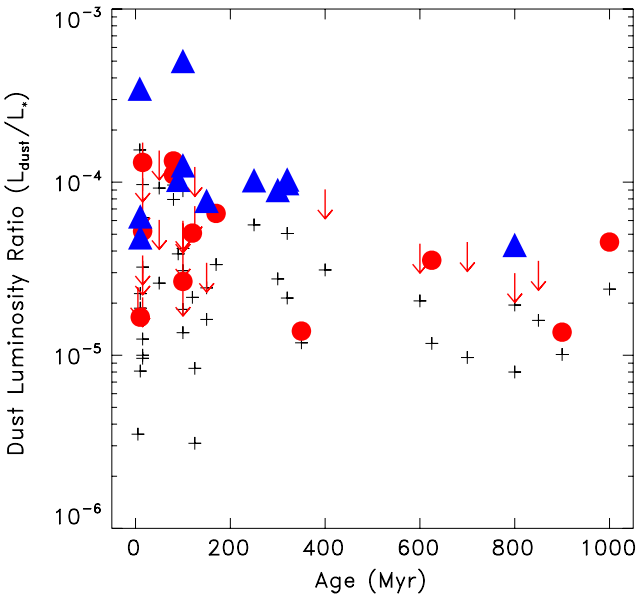

Figure 9. IR fractional dust luminosity vs. age for 45 systems with assigned stellar ages. The solid blue triangles are sources with power-law excesses at IRS wavelengths (all seen with MIPS 70 μm). The red circles are debris systems with IRS blackbody-like excesses that are also detected at 70 μm, while the red down arrows are blackbody-like systems at IRS with MIPS 70 μm upper limits. The black crosses are IRS-only dust luminosity ratios. As in Rieke et al. (2005) and Su et al. (2006), our sample tends to an overall decrease in fractional luminosity with time.

(A color version of this figure is available in the online journal.)

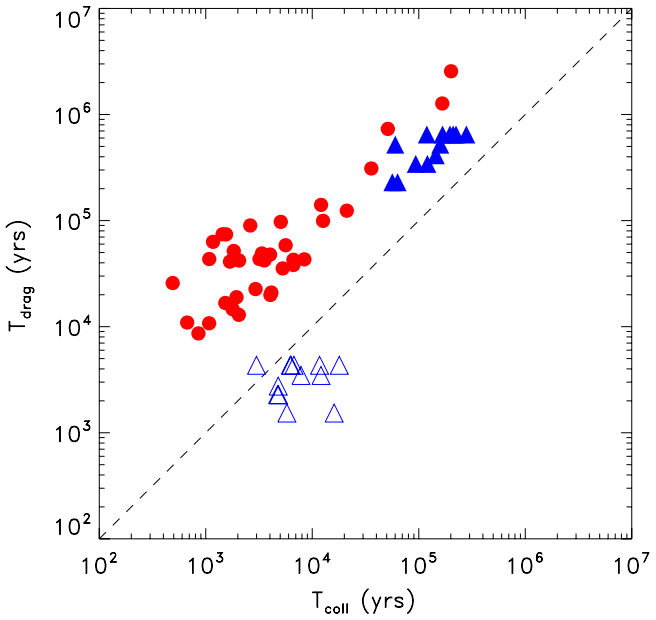

Figure 10. P–R drag timescales vs. collisional timescales for the 50 debris systems and for grains in the vicinity of a_{BOS}. The solid red circles represent the collisionally dominated rings at the IRS wavelengths. The blue triangles are systems with power-law SEDs; solid for distances corresponding to 35 μm emission, and open triangles for distances corresponding to ~10 μm emission. Note all but one power-law system are below the diagonal for timescale ratios corresponding to distances where emission peaks at 10 μm. Transition to a tenuous region where P–R becomes increasingly important appears close to or straddled by the IRS observations.

(A color version of this figure is available in the online journal.)

plotted (bottom) is the median dust distance for the 13 objects better modeled by a power-law flux distribution, where the inner and outer edges are calculated assuming large blackbody grains whose thermal emission peaks from 10 to 35 μm (power-law excess systems may show emission shortward of 10 μm, but we use this limit for consistency in our calculations). A factor of 2 in λ is a factor of 4 in radial distance, so if 70 μm emission originates from grains colder than the ones emitting at 5 to 35 μm, then the cold grains are likely radiating from locations generally 4$\times$ the 35 μm distance in Figure 11.

The study of debris disks with IRS spectroscopy by Chen et al. (2006) used a sample selected at 60 μm and found a large fraction of systems did not have significant excesses at wavelengths short of 30 μm. Su et al. (2006) studied a sample that is not pre-selected in the far infrared, and still the majority of the systems have color temperatures between 24 and 70 μm $\leqslant$ 100 K. Since our sample was selected at 24 μm, it naturally emphasizes the systems with relatively warm material. What is noteworthy, however, is that most of these systems have temperatures from the IRS spectra that are far above expectations from the behavior of other debris disk samples, and that some are even not detected at 70 μm. In addition, there is a striking diversity in disk structure: rings emitting like blackbodies, and radially extended debris emitting in a power-law manner. Almost all of our debris systems emit shortward of 24 μm, at detectable levels typically to about 10 μm. In most cases, the extrapolations of the IRS fits fall below the detections at 70 μm. That is, it appears that these systems have debris distributed over a large range of distances from the star, perhaps in two zones corresponding to warm and cold dust.

In addition to probing different distances, IRS and MIPS 70 μm may sample regions of different composition. In most cases, IRS and MIPS 70 μm temperatures straddle the ice line, such that the material in the warm inner region sampled by IRS is likely to be rocky asteroidal material, whereas the colder outer region seen at MIPS 70 μm can be icy Kuiper Belt-like (primarily composed of ices; Altwegg et al. 1999).

6. DISCUSSION

6.1. Comparison with Previous Work

6.1.1. Selection Effects and the Incidence of Warm Disks

Most previous studies of dust around main-sequence stars have found colder ($T \sim$100 K), icy Kuiper Belt analogs (Beichman et al. 2005b; Bryden et al. 2006; Chen et al. 2006; Plavchan et al. 2009). It has been concluded that disks dominated by warm material are rare (e.g., Smith et al. 2008; Rhee et al. 2008). In contrast, of the 37 systems we find are best fit with black bodies, 32 (86%) have temperatures $\geqslant$ 150 K.

The IRS spectra of debris disks presented by Chen et al. (2006) provide a comparison sample for our study. Their systems were selected on the basis of excess emission at 60 μm; as a result, some were too faint in the 24 μm region for the IRS spectra to provide meaningful constraints on the disk emission. There are 20 late B and A-type stars for which the spectra were adequate to fit a temperature. Two of these systems (ζ Lep and HR 8799), or 10%, have temperatures $\geqslant$ 150 K. According to the binomial theorem, the probability of these two outcomes from a single parent distribution is less than 10^{-8}.

The difference in the two studies undoubtedly arises from selection effects. Because the Chen et al. (2006) sample was selected at 60 μm, it emphasizes cold disks; because ours is selected at 24 μm, it emphasizes warm ones. Since most debris disk samples are selected at 60 or 70 μm, selection effects appear to have led to the conclusion that warm disks are rare.

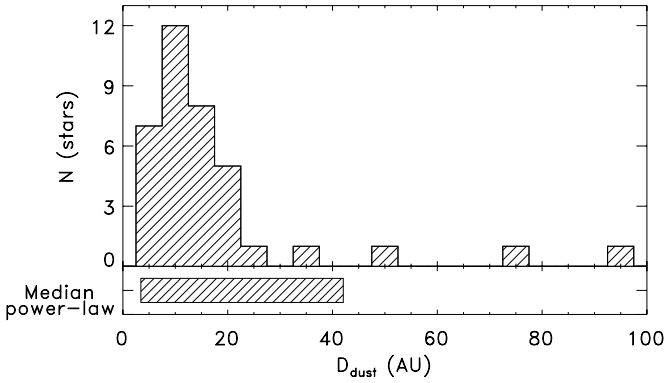

Figure 11. Distance histogram for blackbody sources (top) and distance comparison for systems with a power-law SED (bottom). Blackbody sources have dust radial locations inferred from the best-fit dust temperatures, $T_{\rm dust}$, where the material is assumed to be in thermal equilibrium with the star. The median dust location for blackbody-like systems is 11.9 AU. For 13 systems with power-law SEDs we have estimated an inner and outer edge corresponding to emission at 10 and 35 μm, respectively. The inner and outer edge have median distances of 3.4 and 42.1 AU. Assuming large 70 μm emitting grains are part of colder outer regions, these would be located far to the right of this graph (a factor of 2 in λ is a factor of 4 in $D_{\rm dust}$).

6.1.2. Variety of Disk Structures

Our study adds to the evidence from previous surveys that debris disks come with a large variety of structures. Eight of the systems in our sample have detections or upper limits at 70 μm that demonstrate the turnover of the blackbody fits (HD 23267, 74873, 80950, 87696, 115892, 135454, 136482, 220825). For these systems, it appears that the material emitting near 24 μm lies within a well-defined ring. Seven systems have good blackbody fits toward short wavelengths but a detection at 70 μm moderately above the blackbody (HD 1404, 28355, 159492, 183324, 191174, 215766, 223352). Although there are a variety of explanations for such behavior, it could indicate an extended disk with a sharp inner edge or a gradual density fall off away from the star. HD 98673, 136246 and 192425 have SEDs rising very steeply from 35 to 70 μm, suggesting the presence of a distinct outer cold component Thirteen systems are better fit with power laws than blackbodies. Although the physical conditions producing the power-law systems in our sample are uncertain, we interpret the difference between the blackbody and power-law flux distributions[11] as due to dust distributed in a relatively narrow ring versus a broad extended disk. A theoretically elegant form of filled disk occurs when grains are spiraling in to a star under P–R drag; the simple theory then predicts a power-law SED with an index $\alpha = 1$. In five cases within our sample, α is close to this value (HD 38056, 38206, 79108, 196544, 225200). The remaining eight systems have $\alpha \geqslant 1.4$ (HD 10939, 30422, 70313, 71722, 110411, 138965, 141378, 153053). For them the filled disk probably needs to be maintained by other means.

In contrast to the disks fit by blackbodies at the IRS wavelengths, it is noteworthy that all of the systems with power-law fits are detected at 70 μm. This may suggest the presence of an outer reservoir of cold material which helps to maintain the filled disk.

This variety in behavior has also been indicated by other studies. The FEPS 70 μm Bright Debris Disk survey found $>1/3$ of 37 debris sources to have multiple temperature components (Hillenbrand et al. 2008). Su et al. (2008) find that the SED of gamma Oph, combined with resolved images at 24 and 70 μm, can be fit by a smooth disk extending from 13 to 520 AU. Although only a few debris disks have been resolved well in the infrared, they show a variety of structures, from a compact object of diameter only a few AU for ζ Lep (Moerchen et al. 2007) through a narrow ring for Fomalhaut (Kalas et al. 2006) and inner and outer zones with a narrow inner ring for ϵ Eri (Backman et al. 2009), to photon-pressure-driven large-scale grain outflows for β Pic (Krivov et al. 2000) and Vega (Su et al. 2005).

Similarly, the 70 μm fluxes for the power-law disks show some detections above and some below a simple extrapolation of the short wavelength power law. Overall, a variety of disk architectures is apparent even within the two morphological—blackbody and power law—classifications.

Observational limitations have forced us to treat all debris disks as a closely related family with nearly identical architectures and properties. With the more detailed characterization in this paper and in work such as that cited in the previous paragraph, it is becoming apparent that these previous assumptions were wrong. The broad variety indicates that individual disks are shaped by processes such as planetary resonances sufficiently to strongly influence their infrared outputs.

6.2. Exploring Conditions that May Produce Power-Law Disks

For very small grains, the radiative force can push material outward continuously when it overcomes the gravitational force. Given a stellar luminosity and mass ($L_\star$ and $M_\star$), solid grains of radii smaller than $a_{\rm BOS}$ (Equation (3)) will not sustain a steady orbit and be finally blown out of the system (Artymowicz 1988). The blowout timescales are typically $\sim$10–100 times smaller than the lifetimes for grain destruction mechanisms like P–R drag or collisional grinding. Assuming a steady flow of material, from the equation of continuity we expect that $\tau {\rm R} V_{\rm grain}$ is constant, where $V_{\rm grain}$ is a grain's drift speed. For dust grains undergoing blowout, $V_{\rm grain}$ is constant and $\tau \propto 1/R$, which implies $F_\nu \propto \lambda^{-1}$ via Equation (3). Because all of our power-law systems show energy flux distribution rising with wavelength, implying that $\tau(R)$ increases outward, blowout does not seem a likely explanation for the excess power-law profiles we see.

Because of differences in absorption and radiation efficiencies, a range of temperatures is possible for a distribution of particle sizes within a single-radius ring. While large grains emit at the local blackbody temperature, small particles ($2\pi a_{\rm grain}/\lambda < 1$) can have hotter temperatures at the same location. Resolved debris disks around solar-type stars, for example, are found to have typical dust temperatures about twice the blackbody temperature, implying grain sizes approaching the blowout limit (G. Bryden et al. 2009, in preparation). Similarly, some resolved A star disks have evidence for small hot grains - Vega, with an extended halo of small $\sim$2 μm grains (Su et al. 2005), and HD 32297,[12] with a population of $\sim$0.1 μm grains at temperatures $\sim$3 times blackbody (Fitzgerald et al. 2007; Moerchen et al. 2007). The systems in our sample, however, do not exhibit spectral features that are indicative of small grains. Even with a distribution of dust temperatures spanning a factor of 2 in temperature at a single orbital location, we cannot produce excess flux close to a power law over the IRS wavelengths.

Continuous disks of slope $\alpha\sim$ 1 may simply represent a population of unseen parent bodies that collisionally replenish dust

[11] In a few power-law cases the excesses appear to rise faster than a power law at wavelengths longward of $\sim$ 30 μm.

[12] HD 32297 is much younger than the majority of the targets studied here. Its small grains may be primordial.

which is redistributed radially by P–R drag (Burns et al. 1979). But for power-law systems of slope $\alpha > 1$, our results may suggest a different distribution of parent bodies or planetesimals. Given that these systems are 5–1000 million years old, primordial molecular gas is long gone, and small dust particles must have been generated in relatively recent collisions between parent bodies. From our grain timescale examination (Section 5.3) involved in dust production and removal, we find all systems to be collisionally dominated at the blackbody distances and at distances corresponding to 35 μm emission for the 13 power laws. Hence, the dust and the parent bodies are expected to be co-located. However, the majority of IRS power-law systems shift from collisional at the longer IRS wavelengths to P–R drag dominated at the inner regions corresponding to 15 μm emission; the IRS wavelength range straddles the location where grains pass from a dense collisional environment to a state of angular momentum loss and migration toward the star.

7. SUMMARY AND CONCLUSIONS

This paper presents newly obtained IRS spectra of previously identified debris disks around 50 main-sequence A and late B stars. The spectra are combined with MIPS photometry at 24 μm and 70 μm to obtain a more complete picture of the dust distribution around these stars than is obtained from the photometry alone.

We find that the 5–35 μm IRS spectra alone fall into two rather distinct groups, blackbody-like spectra and power-law spectra. The identification of these two classes and the study of the disks with warm power-law spectra, which make up ∼25% of the sample, is the major new result presented here. Although the distinction between power law and blackbody may be somewhat arbitrary for a few of the stars, ancillary data suggest very strongly that these are two separate classes of debris systems. In particular, 100% of the power-law systems are also detected at 70 μm, while less than half of the blackbody systems are detected to comparable sensitivity levels at this wavelength. For most power-law and blackbody-like excess systems, the detected 70 μm flux does not fall on an extrapolation of the SED determined from the IRS data alone. This suggests that the 70 μm radiation comes from a different dust distribution from that seen at the shorter wavelengths, and more complex models are required to explain these systems' full SEDs. By analogy with our own solar system, it is tempting to state that the IRS samples material in an asteroidal zone (T∼200 K; Low et al. 1984) while the 70 μm radiation arises primarily from an outer region likely similar to the Kuiper Belt (T∼50 K; Jewitt & Luu 2004).

The sample studied here differs from most other debris disk samples because it was based on 24 μm detections. In addition, assuming the 70 μm emission is radiated via large cold grains located in regions further out from the star than those implied by the warm IRS excess, the IRS spectra allow us to separate dust population emitting shortward and longward of ∼50 μm. For this 24 μm selected sample, we found that the minimum stellar luminosity reradiated shortward of 50 μm is generally greater than the minimum reradiated longward of 50 μm. For those disks detected at 70 μm, the mass implied from the 70 μm flux is ∼1–2 orders of magnitude greater than that required to produce the flux seen at the shorter IRS wavelengths.

Simple considerations suggest that the blackbody-like IRS spectra arise from a dust distribution that is confined to a small radial zone around the star. The observed blackbody temperatures, 70–324 K, indicate that the radii of these annuli vary between 93 and 5 AU. By contrast, the power-law excess spectra require dust that is distributed over a wide radial range (typically ∼3 to ∼40 AU). If the power-law spectra are interpreted in this fashion, we find that at the outer radii, sampled by wavelengths around 35 μm, grain–grain collisions are the main loss mechanism for the particles, while at smaller distances, sampled by wavelengths around 10 μm, P–R becomes increasingly important. By contrast, the blackbody systems are always collision-dominated.

If not transient structures, we suggest that the blackbody spectra, specially those where the single-temperature blackbody fits agree with 70 μm photometry, are likely to arise from systems where one or more planetary objects embedded within or adjacent to the dust distribution govern the dynamics of the observed debris and its parent bodies. Shepherding by planets is a natural way to maintain the dust in a narrow ring. The power-law spectra may be attributed to planet-poor systems where the material is free to migrate radially. This is consistent both with the transition from collision to drag-dominated behavior referred to above and with the detection of all of the power-law excess systems at 70 μm, which is suggestive of communication between the warm asteroidal and Kuiper components of the system. Detailed modeling will be the next step required to investigate this hypothesis.

This work is based on observations made with the *Spitzer Space Telescope*, which is operated by the Jet Propulsion Laboratory, California Institute of Technology, under NASA contract 1407. Development of MIPS was funded by NASA through the Jet Propulsion Laboratory, subcontract 960785. This work was also partially supported by contract 1255094 from Caltech/JPL to the University of Arizona. Part of the research described in this publication was carried out at the Jet Propulsion Laboratory, California Institute of Technology, under a contract with the National Aeronautics and Space Administration. This publication makes use of data products from the Two Micron All Sky Survey (2MASS) and from the SIMBAD Web site.

APPENDIX A

DERIVATION OF CONTINUOUS DISK PROPERTIES–POWER-LAW DERIVATIONS

Under the assumption of simple grain emissivities, disks with power-law flux distributions can readily be related to power-law density distributions which can then be integrated to obtain overall disk properties such as its luminosity and mass. Here, we derive expressions to translate from the observed flux distribution to the underlying disk characteristics.

We start our derivation with a smooth disk whose vertical optical depth varies with radius as a power law with exponent β

$$\tau(R) = \tau_{1\,\mathrm{AU}} R_{\mathrm{AU}}^{\beta}, \tag{A1}$$

where R_{AU} is the orbital location in AU and $\tau_{1\,\mathrm{AU}}$ is the vertical depth at 1 AU. (Note that the slope of the disk thickness, β, is related to but different from the slope of the flux density, α.) For a disk surrounding a star of luminosity $L_{\star}$, the fraction of the star's luminosity absorbed by each radial shell of width ΔR is

$$\frac{\Delta L_{\mathrm{dust}}}{L_{\star}} = \tau(R)\frac{\Delta R}{2R} = \tau_{1\,\mathrm{AU}} R_{\mathrm{AU}}^{\beta}\frac{\Delta R}{2R}. \tag{A2}$$

Table 4
IRAS 25 μm Selected and Faint A Star Sample

Name	Spectral Type	V (mag)	Distance (pc)	18 μm $F_{\rm IRS}/F_\star$	24 μm $F_{\rm IRS}/F_\star$	$T_{\rm dust}$ (K)	$L_{\rm dust,IRS}/L_\star$	AOR
HD12216[a]	A2V	3.95	49.7	...	...	...	...	14146048
HD122408[a]	A3V	4.24	66.9	...	...	...	...	14145280
HD17573[a]	B8Vn	3.61	48.9	1.26	1.93	206	1.9E-05	14145024
HD178253[a]	A2Va	4.10	39.8	1.25	2.08	202	2.3E-05	14145536
HD181869[a]	B8V	3.95	52.1	...	...	...	...	14146560
HD56537[a]	A3V	3.58	28.9	...	...	...	...	14144768
HD79469[a]	B9.5V	3.88	39.5	...	...	...	...	14145792
CD-48 3539	A0	10.59	...	...	...	...	...	14155008
CD-48 3540	...	9.36	...	...	...	...	...	14152704
CD-48 3541	...	9.67	...	...	...	...	...	14153216
CD-48 3575	...	10.92	...	1.36	...	...	...	14154240
CD-48 3578	...	11.09	...	...	...	...	...	14156800
CD-49 3371	...	10.72	...	1.57	...	...	...	14153984
CD-49 3390	...	10.93	...	1.57	...	...	...	14157056
CPD-48 1496	...	10.94	...	1.85	...	...	...	14153472
CPD-48 1532	...	10.78	...	...	...	...	...	14152448
CPD-60 1007	A8V	10.88	...	1.27	...	...	...	14156544
CPD-60 1032	...	10.40	...	...	...	...	...	14156032
cpd-60 975	Av...	8.92	...	...	...	...	...	14157312
CPD-60 983	A6V	10.50	...	...	...	...	...	14154496
CPD-60 986	A2V	9.95	...	1.25	...	...	...	14154752
CPD-60 994	A3V	10.80	...	1.41	...	...	...	14156288
GSC 08911-03279	...	11.00	...	1.24	...	...	...	14155776
HD68114	A0V	9.41	...	...	...	...	...	14155520
HD68294	A0V	9.12	...	...	...	...	...	14152960
HD68420	A3V	9.84	...	2.03	3.10	201	1.2E-04	14152192
HD68558	A0V	9.80	...	...	...	...	...	14155264
HD68698	A1V	9.86	...	1.46	...	...	...	14153728
NSV17775	A1V	9.88	...	1.70	4.45	161	9.0E-05	14151936
Cl* NGC 2422 pms 1152	...	10.00	...	...	...	...	...	14158080
Cl* NGC 2422 pms 1158	...	9.02	...	...	...	...	...	14158592
Cl* NGC 2422 pms 1172	...	10.69	...	1.21	...	...	...	14157824
Cl* NGC 2422 pms 1173	...	10.40	...	...	...	...	...	14159104
Cl* NGC 2422 pms 1182	...	11.02	...	...	...	...	...	14157568
Cl* NGC 2422 pms 1204	...	11.53	...	...	...	...	...	14158336
Cl* NGC 2422 pms 921	...	11.50	...	1.21	...	...	...	14158848
Cl* NGC 2516 DAC 11A	...	10.61	...	...	...	...	...	14160128
Cl* NGC 2516 DAC 227	...	11.20	...	...	...	...	...	14159872
Cl* NGC 2516 DAC 232	...	11.37	...	...	...	...	...	14159360
Cl* NGC 2516 DAC 516	...	11.17	...	...	...	...	...	14159616
HD60856[b]	B5V	7.94	56.8	1.33	2.39	215	5.3E-05	14151424
HD60995	B8/B9V	8.67	...	1.63	2.27	226	5.0E-05	14151680

Notes.
[a] *IRAS* 25 μm selected target.
[b] With hydrogen free–free emission features.

The specific flux from each shell is

$$\Delta F_{\nu,\rm dust} = \frac{B_\nu(T_{\rm dust})}{4R^2\sigma T_{\rm dust}^4}\Delta L_{\rm dust} = \frac{B_\nu(T_{\rm dust})}{8R^2\sigma T_{\rm dust}^4} L_\star \tau_{1\,\rm AU} R_{\rm AU}^{\beta-1}\Delta R_{\rm AU}, \tag{A3}$$

where R is the distance to the star, B_ν is the Planck function for blackbody emission and, $T_{\rm dust}(R)$ is the dust temperature as a function of distance from the central star. The dust temperature depends on the grain emissivity, with small grains hotter than the local blackbody temperature. Assuming large blackbody grains, the dust temperature as a function of radius is $T_{\rm dust} = (L_\star/16\pi\sigma R^2)^{1/4} \sim eq\, R_{\rm AU}^{-1/2}(L_\star/L_\odot)^{1/4}$ 280 K. With this relationship between R and $T_{\rm dust}$ we can then convert from a radial function to one with just temperature dependence:

$$\Delta F_{\nu,\rm dust} = \frac{L_\star \tau_{1\,\rm AU}}{4d^2}\left(\frac{T_{1\,\rm AU}}{T_{\rm dust}}\right)^{2\beta}\frac{B_\nu(T_{\rm dust})\Delta T_{\rm dust}}{\sigma T_{\rm dust}^5}, \tag{A4}$$

where $T_{1\,\rm AU} = (L_\star/16\pi\sigma \mathrm{AU}^2)^{1/4} = (L_\star/L_\odot)^{1/4}$ 280 K. Integrating this equation over the entire disk, we have

$$F_{\nu,\rm dust} = \frac{L_\star \tau_{1\,\rm AU} T_{1\,\rm AU}^{2\beta}}{4d^2\sigma}\int \frac{B_\nu(T_{\rm dust})}{T_{\rm dust}^{5+2\beta}} dT_{\rm dust}. \tag{A5}$$

The integral of the Planck function times a power law can be reduced to a Riemann zeta function, ζ, which is close to unity for the slopes considered here. The total disk flux then becomes

$$F_{\nu,\rm dust} = \frac{L_\star \tau_{1\,\rm AU}}{2d^2\sigma}\frac{k^4}{h^3\nu c^2}\left(\frac{kT_{1\,\rm AU}}{h\nu}\right)^{2\beta}(3+2\beta)! \tag{A6}$$

$$\approx 1\,\mathrm{mJy}\,\frac{0.46^{2\beta}(3+2\beta)!}{6}\left(\frac{L_\star}{L_\odot}\right)^{1+\beta/2}\left(\frac{d}{50\,\mathrm{pc}}\right)^{-2} \times \left(\frac{\tau_{1\,\rm AU}}{10^{-5}}\right)\left(\frac{\lambda}{24\,\mu\mathrm{m}}\right)^{1+2\beta} \tag{A7}$$

or, relative to the stellar flux, the disk flux is

$$\frac{F_{\nu,\mathrm{dust}}}{F_{\nu,*}} \approx 0.32 \frac{0.46^{2\beta}(3+2y)!}{6} \left(\frac{L_\star}{L_\odot}\right)^{\beta/2} \left(\frac{T_\star}{10{,}000\,\mathrm{K}}\right)^3 \times \left(\frac{\tau_{1\,\mathrm{AU}}}{10^{-5}}\right) \left(\frac{\lambda}{24\ \mu\mathrm{m}}\right)^{3+2\beta}. \quad \text{(A8)}$$

Given our observations of flux strength ($\frac{F_{\nu,\mathrm{dust}}}{F_{\nu,*}}$) and slope ($\alpha$), we want to determine the underlying distribution of dust thickness (τ with slope β). From the wavelength dependence of Equation (A7), we see that the flux slope α is equal to 1+2β. With this substitution, we then rearrange Equation (A8) to solve for τ as a function of radius

$$\tau \approx 3 \times 10^{-5} \left.\frac{F_{\nu,\mathrm{dust}}}{F_{\nu,*}}\right|_{24\,\mu\mathrm{m}} \frac{6}{0.46^{\alpha-1}(\alpha+2)!} \left(\frac{L_\star}{L_\odot}\right)^{(1-\alpha)/4} \times \left(\frac{T_\star}{10{,}000\,\mathrm{K}}\right)^{-3} R_{\mathrm{AU}}^{(\alpha-1)/2}. \quad \text{(A9)}$$

This distribution of area can be integrated to get the overall mass of dust in the disk.

$$M_{\mathrm{dust,PL}} = \int 2\pi R \Sigma \mathrm{d}R = 2\pi \int \frac{4 a_g \rho_g}{3} \tau R \mathrm{d}R = \frac{16\pi a_g \rho_g \mathrm{AU}^2}{3(\alpha+3)} \tau_{1\,\mathrm{AU}} R_{\mathrm{AU,max}}^{(\alpha+3)/2}, \quad \text{(A10)}$$

where a_g and ρ_g are the typical grain radius and density. Note that some outer edge to the disk, R_{max}, must be specified, otherwise the disk size and mass are infinite. For IRS observations extending out to a wavelength of ~35 μm, we know that the range of disk temperatures goes down to at least 100 K, if not colder. This corresponds to a minimum disk size of

$$R_{\mathrm{AU,max}} \gtrsim 10\ \mathrm{AU} \left(\frac{L_\star}{L_\odot}\right)^{1/2}. \quad \text{(A11)}$$

So the minimum dust mass from IRS observations alone is then

$$M_{\mathrm{dust,PL}} > 10^{22} g \left(\frac{10^{(\alpha-1)/2}}{\alpha+3}\right) \left(\frac{\tau_{1\,\mathrm{AU}}}{10^{-5}}\right) \left(\frac{a_g}{10\ \mu\mathrm{m}}\right) \times \left(\frac{\rho_g}{3\ \mathrm{g\ cm^{-3}}}\right) \left(\frac{L_\star}{L_\odot}\right)^{(\alpha+3)/4}. \quad \text{(A12)}$$

Values for the dust mass lower limits are given in Table 3 under the assumption that the typical grain size is equal to the radiation blowout limit (Equation (3)). Two masses are given in the table—the minimum from IRS observations alone and the larger mass contained by the disk extending out to 70 μm.

APPENDIX B

ADDITIONAL SPECTRA OF LOWER QUALITY

There are an additional 35 fainter sources for which we have lower S/N IRS spectra (5.2–21.3 μm) and 7 *IRAS* 25 μm selected objects in *Spitzer* PID 20132. Based on their preliminary MIPS 24 μm fluxes, 11 stars were found to be bright enough to warrant observations over all IRS wavelengths. We find six of these sources have detectable excess flux ratios at both 18 μm and 24 μm (Table 4). One of these sources (HD60856) has excess flux emission showing hydrogen free–free emission features. We confirm warm excess for only two of the seven *IRAS* 25 μm selected objects. The remaining 31 stars were only observed with IRS out to 21 μm (these stars were not expected to have sufficient S/N at 24 μm). Eleven of the 31 stars have 18 μm excesses at least 20% above that expected from the photosphere with an uncertainty of =< 10%. Unlike the stars discussed in the main text, these sources were not observed with MIPS at 70 μm.

REFERENCES

Altwegg, K., Balsiger, H., & Geiss, J. 1999, Space Sci. Rev., 90, 3
Artymowicz, P. 1988, ApJ, 335, L79
Backman, D. E., Dasgupta, A., & Stencel, R. E. 1995, ApJ., 450, L35
Backman, D. E., & Paresce, F. 1993, in Protostars and Planets III, ed. E. H. Levy & J. I. Lunine (Tucson, AZ: Univ. Arizona Press), 1253
Backman, D. E., Witteborn, F. C., & Gillett, F. C. 1992, ApJ, 385, 670
Backman, D., et al. 2009, ApJ, 690, 1522
Beichman, C. A., et al. 2005a, ApJ, 626, 1061
Beichman, C. A., et al. 2005b, ApJ, 622, 1160
Bohren, C. F., & Huffman, D. R. 1983, Absorption and Scattering of Light by Small Particles, ed. C. F. Bohren & D. R. Huffman (New York: Wiley)
Bryden, G., et al. 2006, ApJ, 636, 1098
Burns, J. A., Lamy, P. L., & Soter, S. 1979, Icarus, 40, 1
Chen, C. H., et al. 2005, ApJ, 634, 1372
Chen, C. H., et al. 2006, ApJS, 166, 351
Chiang, E., Kite, E., Kalas, P., Graham, J. R., & Clampin, M. 2009, ApJ, 693, 734
Cutri, R. M., et al. 2003, VizieR Online Data Catalog, 2246
Dohnanyi, J. S. 1968, in IAU Symp. 33, Physics and Dynamics of Meteors (Dordrecht: Kluwer), 486
Dominik, C., & Decin, G. 2003, ApJ, 598, 626
Engelbracht, C. W., et al. 2007, PASP, 119, 994
Fitzgerald, M. P., Kalas, P. G., & Graham, J. R. 2007, ApJ, 670, 557
Fixsen, D. J., & Dwek, E. 2002, ApJ, 578, 1009
Gautier, T. N. III, et al. 2007, ApJ, 667, 527
Golimowski, D. A., et al. 2006, AJ, 131, 3109
Gordon, K. D., et al. 2007, PASP, 119, 1019
Gustafson, B. A. S. 1994, Annu. Rev. Earth Planet. Sci., 22, 553
Heap, S. R., et al. 2000, ApJ, 539, 435
Hillenbrand, L. A., et al. 2008, ApJ, 677, 630
Houck, J. R., et al. 2004, ApJS, 154, 18
Jewitt, D. C., & Luu, J. 2004, Nature, 432, 731
Jura, M., et al. 1995, ApJ, 445, 451
Jura, M., et al. 1998, ApJ, 505, 897
Kalas, P., Graham, J. R., & Clampin, M. 2005, Nature, 435, 1067
Kalas, P., Graham, J. R., Clampin, M. C., & Fitzgerald, M. P. 2006, ApJ, 637, L57
Koerner, D. W., Ressler, M. E., Werner, M. W., & Backman, D. E. 1998, ApJ, 503, L83
Krivov, A. V., Mann, I., & Krivova, N. A. 2000, A&A, 362, 1127
Lawler, S. M., et al. 2009, ApJ, submitted
Low, F. J., et al. 1984, ApJ, 278, L19
Minato, T., Köhler, M., Kimura, H., Mann, I., & Yamamoto, T. 2006, A&A, 452, 701
Moerchen, M. M., Telesco, C. M., De Buizer, J. M., Packham, C., & Radomski, J. T. 2007, ApJ, 666, L109
Plavchan, P., et al. 2009, ApJ, in press (arXiv:0904.0819)
Rhee, J. H., Song, I., & Zuckerman, B. 2008, ApJ, 675, 777
Rieke, G. H., et al. 2004, ApJS, 154, 25
Rieke, G. H., et al. 2005, ApJ, 620, 1010
Schneider, G., et al. 1999, ApJ, 513, L127
Smith, R., Wyatt, M. C., & Dent, W. R. F. 2008, A&A, 485, 897
Stapelfeldt, K. R., et al. 2004, ApJS, 154, 458
Su, K. Y. L., et al. 2005, ApJ, 628, 487
Su, K. Y. L., et al. 2006, ApJ, 653, 675
Su, K. Y. L., et al. 2008, ApJ, 679, L125
Trilling, D., et al. 2008, ApJ, 674, 1086
Werner, M., Fazio, G., Rieke, G., Roellig, T. L., & Watson, D. M. 2006, ARA&A, 44, 269
Werner, M. W., et al. 2004, ApJS, 154, 1
Wyatt, M. C. 2005, A&A, 433, 1007
Wyatt, M. C., Greaves, J. S., Dent, W. R. F., & Coulson, I. M. 2005, ApJ, 620, 492
Wyatt, M. C., et al. 1999, ApJ, 527, 918
Wyatt, M. C., et al. 2007, ApJ, 663, 365